Fault-magma interactions during early continental rifting: Seismicity of the Magadi-Natron-Manyara basins, Africa

A. Weinstein, S. J. Oliva, C. J. Ebinger, S. Roecker, Christel Tiberi, M. Aman, C. Lambert, E. Witkin, Julie Albaric, Stephanie Gautier, et al.

AGU PUBLICATIONS

Geochemistry, Geophysics, Geosystems

RESEARCH ARTICLE
10.1002/2017GC007027

Key Points:
- Lower crustal earthquakes along projections of steep border faults
- Local stress field rotation facilitates strain transfer from border fault to central zone of magma intrusion
- Volatile release from magma intrusion localizes strain in early-stage rift systems

Supporting Information:
- Supporting Information S1

Correspondence to:
C. J. Ebinger,
cebinger@tulane.edu

Citation:
Weinstein, A., et al. (2017), Fault-magma interactions during early continental rifting: Seismicity of the Magadi-Natron-Manyara basins, Africa, *Geochem. Geophys. Geosyst.*, *18*, 3662–3686, doi:10.1002/2017GC007027.

Received 23 MAY 2017
Accepted 10 AUG 2017
Accepted article online 21 AUG 2017
Published online 30 OCT 2017

Fault-magma interactions during early continental rifting: Seismicity of the Magadi-Natron-Manyara basins, Africa

A. Weinstein[1], S. J. Oliva[2], C. J. Ebinger[2], S. Roecker[3], C. Tiberi[4], M. Aman[1], C. Lambert[1], E. Witkin[1], J. Albaric[5], S. Gautier[4], S. Peyrat[4], J. D. Muirhead[6], A. N. N. Muzuka[7], G. Mulibo[8], G. Kianji[9], R. Ferdinand-Wambura[8], M. Msabi[8], A. Rodzianko[3], R. Hadfield[1], F. Illsley-Kemp[10], and T. P. Fischer[11]

[1]Earth and Environmental Sciences, University of Rochester, Rochester, New York, USA, [2]Earth and Environmental Sciences, Tulane University, New Orleans, Louisiana, USA, [3]Earth and Environmental Sciences, Rensselaer Polytechnic Institute, Troy, New York, USA, [4]Géosciences Montpellier, Université de Montpellier, Montpellier, France, [5]Laboratoire Chrono-Environnement, Bourgogne Franche-Comté University, Besançon, France, [6]Department of Earth Sciences, Syracuse University, Syracuse, New York, USA, [7]Nelson Mandela African Institution of Science and Technology, Arusha, Tanzania, [8]Department of Geology, University of Dar-es-Salaam, Dar Es Salaam, Tanzania, [9]Department of Geology, University of Nairobi, Nairobi, Kenya, [10]Southampton University, Southampton, UK, [11]Department of Earth Sciences, University of New Mexico, Albuquerque, New Mexico, USA

Abstract Although magmatism may occur during the earliest stages of continental rifting, its role in strain accommodation remains weakly constrained by largely 2-D studies. We analyze seismicity data from a 13 month, 39-station broadband seismic array to determine the role of magma intrusion on state-of-stress and strain localization, and their along-strike variations. Precise earthquake locations using cluster analyses and a new 3-D velocity model reveal lower crustal earthquakes beneath the central basins and along projections of steep border faults that degas CO_2. Seismicity forms several disks interpreted as sills at 6–10 km below a monogenetic cone field. The sills overlie a lower crustal magma chamber that may feed eruptions at Oldoinyo Lengai volcano. After determining a new M_L scaling relation, we determine a *b*-value of 0.87 ± 0.03. Focal mechanisms for 65 earthquakes, and 13 from a catalogue prior to our array reveal an along-axis stress rotation of ~60° in the magmatically active zone. New and prior mechanisms show predominantly normal slip along steep nodal planes, with extension directions ~N90°E north and south of an active volcanic chain consistent with geodetic data, and ~N150°E in the volcanic chain. The stress rotation facilitates strain transfer from border fault systems, the locus of early-stage deformation, to the zone of magma intrusion in the central rift. Our seismic, structural, and geochemistry results indicate that frequent lower crustal earthquakes are promoted by elevated pore pressures from volatile degassing along border faults, and hydraulic fracture around the margins of magma bodies. Results indicate that earthquakes are largely driven by stress state around inflating magma bodies.

1. Introduction

Magmatism during continental rifting creates new continental crust through dike and sill intrusion into existing crust, and through lavas and constructs at the surface [e.g., *Thybo and Artemieva*, 2013; *Desissa et al.*, 2013; *Ebinger et al.*, 2013; *Lee et al.*, 2016]. Although the greatest amount of strain during intense rifting events is accommodated by magma intrusion [e.g., *Grandin et al.*, 2009; *Calais et al.*, 2008; *Belachew et al.*, 2011], the relative importance of magma intrusion in time-averaged strain accommodation remains only loosely quantified in early-stage rift zones [e.g., *Biggs et al.*, 2009; *Ebinger et al.*, 2013; *Muirhead et al.*, 2015, 2016].

The aims of our study are to evaluate the role of magma intrusion during early-stage rifting in a region of active volcanism, dike intrusion, and volumetrically large degassing along fault zones: the southern sector of the Eastern (Gregory) rift system, Africa [e.g., *Calais et al.*, 2008; *Albaric et al.*, 2014; *Lee et al.*, 2016] (Figure 1 and supporting information Figure SM1). A sequence of damaging earthquakes, dike intrusions, and eruption at Oldoinyo Lengai volcano in 2007–2008 [*Baer et al.*, 2008; *Calais et al.*, 2008; *Biggs et al.*, 2009], and a possible intrusion in the Magadi basin in 1998 [*Ibs-von Seht et al.*, 2001] suggest links between

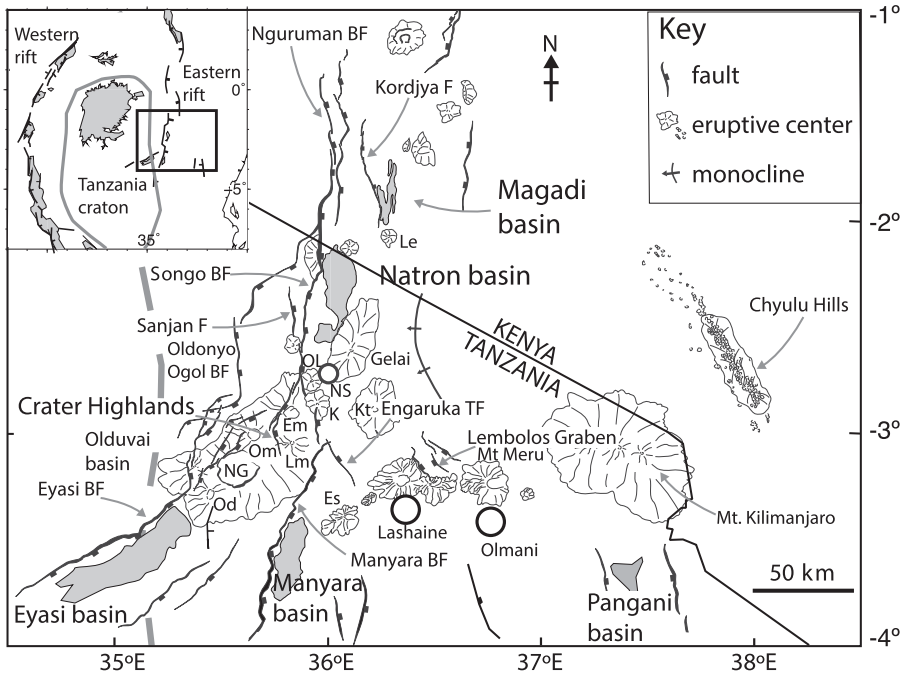

Figure 1. Simplified map of major faults and composite volcanoes in the southern sector of the Eastern rift, sometimes referred to as the North Tanzania Divergence, after *Foster et al.* [1997], *Le Gall et al.* [2008], *Ebinger and Scholz* [2012], and *Muirhead et al.* [2016]. Inset shows location with respect to major faults of Eastern and Western rifts, and thick Archaean craton (details in supporting information Figure S1). Labeled features refer to large normal faults discussed in the text. Our focus is the Magadi, Natron, and Manyara basins, and their uplifted flanks, including the Crater Highlands horst. The active carbonatite volcano Oldoinyo Lengai lies in the center (OL), and Mts. Meru and Kilimanjaro lie to the southeast. Naibor Soito monogenetic cone complex indicated by circle labeled NS, which hosts the Pello Hill, Eledoi, and Naibor Soito xenolith sites; Lashaine and Olmani are other xenolith localities. BF = border fault; F = fault. Volcanoes mentioned in text are from N to S: Og = Olorgesailie; Le = Lenderut; K = Kerimasi; Kt = Kitumbeine; Em = Embagai; Om = Olmoti; Lm = Loolmalasin; NG = Ngorongoro crater; Od = Oldeani; Es = Essimingor. Other volcano names in supporting information Figure S2.

earthquake activity, magmatism, and the movement of volatile-rich fluids in the crust. Earthquakes at depths of 20–35 km have been documented in this sector [e.g., *Ibs-von Seht et al.*, 2001; *Mulibo and Nyblade*, 2009; *Yang and Chen*, 2010; *Albaric et al.*, 2014], offering insights into crustal rheology and magmatic processes.

The fluid transfer to the continental plate may have several consequences. Specifically, mineral physics, seismic and magnetotelluric (MT) imaging, and xenoliths provide increasing evidence that hydration state and high partial pressures of CO_2 as well as temperature significantly influence the rheology, density, seismic velocity, and thermodynamics of minerals [e.g., *Vauchez et al.*, 2005; *Schmandt and Humphreys*, 2010; *Wada et al.*, 2012; *Selway et al.*, 2014; *Guerri et al.*, 2015; *Jones et al.*, 2015]. Magmatic fluids (magma, brines) and exsolved gas phases may modify the frictional properties of fault zones [e.g., *Niemeijer and Spiers*, 2005]. In addition, the topographic relief of early-stage rift basins and flanks produces pressure gradients that may guide the spatial distribution of magma intrusions [*Maccaferri et al.*, 2014]. Heat transfer and the migration of magmatic fluids and exsolved gases through the thinning plate beneath rift zones may, therefore, play a key role in strain localization during early-stage rifting [e.g., *Buck*, 2004; *Keir et al.*, 2006a; *Muirhead et al.*, 2016].

The 39-seismometer Continental Rift And Fluid-Tectonic Interaction (CRAFTI) and the Continental Lithospheric Breakup in East Africa (CoLiBrEA) combined seismic array was deployed across the Kenya-Tanzania border between January 2013 and December 2014 to evaluate the time-space distribution and kinematics of crustal strain across and between three rift basins of different age and volume of eruptive products: Magadi, Natron, and Manyara basins, and their flanking uplifts and eruptive centers (Figures 1 and 2 and supporting information Figure SM2). Companion papers by *Roecker et al.* [2017] and *Plasman et al.* [2017] constrain the modification of crust and uppermost mantle by magmatism, fluid release, and crustal stretching, and together they offer new insights into the unusual lower crustal earthquakes in this rift sector. The 3427 earthquakes from the CRAFTI-CoLiBrEA array are relocated using a 3-D velocity model derived from

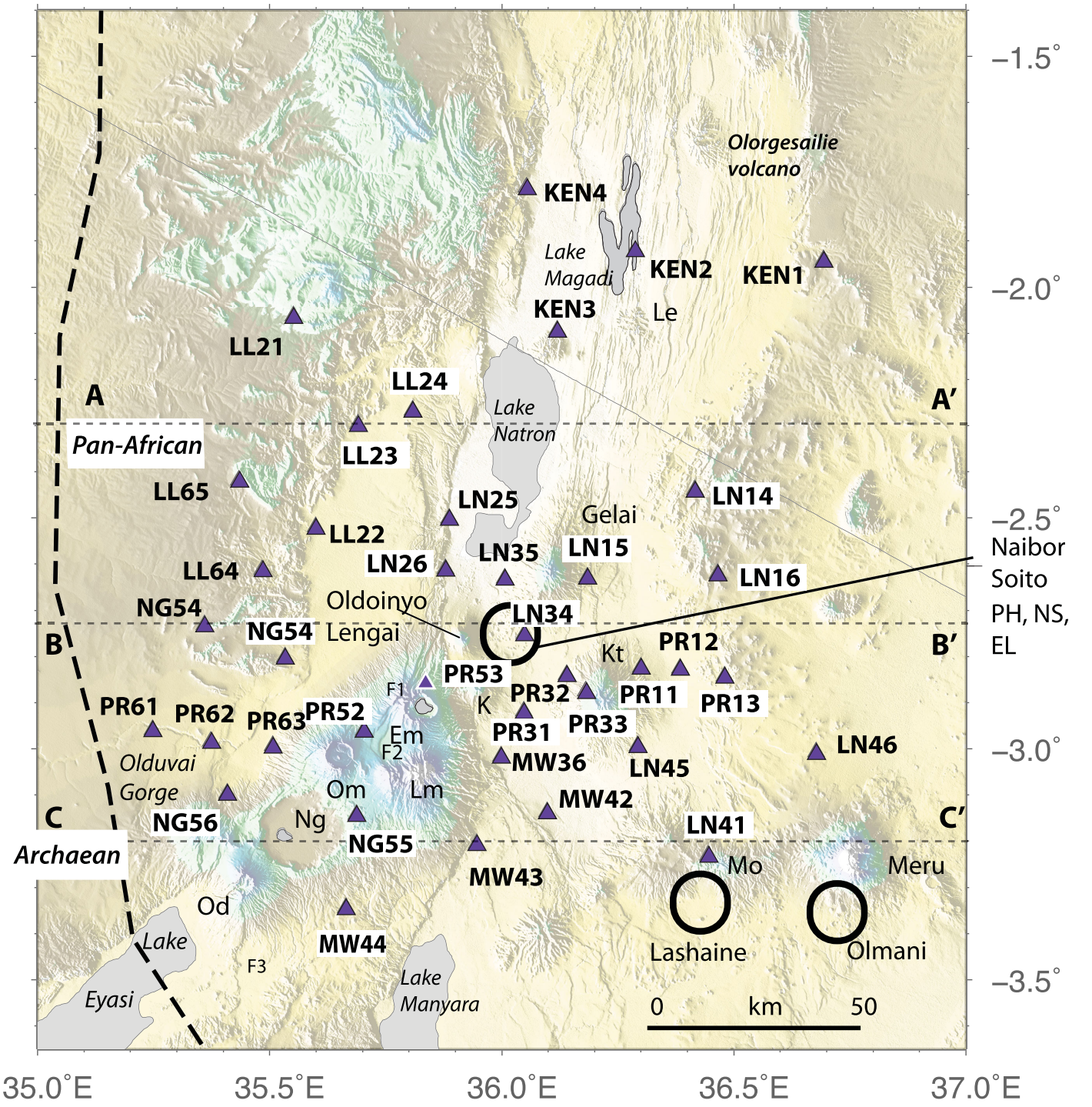

Figure 2. Focus area showing station names of CRAFTI-CoLiBrEA seismometers deployed in northern Tanzania and southern Kenya between 13 January 2013 and 8 December 2014 (purple triangles) with respect to Miocene-Recent eruptive centers and xenolith localities (black circles). Circle labeled Naibor Soito encloses the Naibor Soito monogenetic cone complex that hosts the Pello Hill (PH), Eledoi (E), and Naibor Soito (NS) mantle and crustal xenolith localities [*Mansur et al*., 2014]. Lashaine and Naibor Soito host Archaean lower crustal xenoliths, indicating that the Archaean-Pan-African contact dips eastward [*Mansur et al*., 2014]. Archaean-Pan-African surface contact from *Manya and Maboko* [2003]. Dashed lines A–A′ (2.3°S), B–B′ (2.72°S), and C–C′ (3.2°S) correspond to the cross sections in Figure. 9. F1–F3 are unnamed faults referred to in text.

joint inversion of *P* and *S* arrivals, ambient noise tomography, and gravity data [*Roecker et al*., 2017], and double-difference cluster analyses of cross-correlated waveforms and manual picks. First-motion focal mechanism solutions provide information on kinematics of border and intrabasinal faults, and stress state

around magma bodies. We estimate the extension direction and strain rate from analyses of earthquakes detected on the CRAFTI-CoLiBrEA array, earlier local arrays [*Ibs-von Seht et al.*, 2001; *Mulibo and Nyblade*, 2009; *Albaric et al.*, 2010] and from events detected regionally and teleseismically [e.g., *Dziewonski et al.*, 1981; *Yang and Chen*, 2010; *Craig et al.*, 2011]. We then compare patterns with those of time-integrated patterns of faulting and magmatism [*Foster et al.*, 1997; *Le Gall et al.*, 2008; *Muirhead et al.*, 2015].

2. Background

Active faulting and magmatism occur across a large part of the African continent above one of Earth's largest mantle upwellings, the African Superplume [e.g., *Nyblade and Robinson*, 1994; *Mulibo and Nyblade*, 2013; *Kendall and Lithgow-Bertelloni*, 2016]. The Eastern (Gregory) rift marks the divergent plate boundary between the slowly opening ($\leq$6 mm yr^{-1}) Nubia and Somalia plates [e.g., *Saria et al.*, 2013; *Birhanu et al.*, 2016] (Figure 1 and supporting information Figure SM1). The Eastern rift splays into a broad zone of $\sim$80 km-long, seismically active faults and eruptive centers at its southern termination in Tanzania, and it transects Archaean lithosphere (Figure 1). Based on the National Earthquake Information Center (NEIC) catalogue from 1976 to present, this southernmost sector of the Eastern rift is its most seismically active part, with damaging earthquakes, and frequent volcanic eruptions at the carbonatitic volcano Oldoinyo Lengai [*Dawson*, 1992; *Baer et al.*, 2008; *Kervyn et al.*, 2010] (Figures 1 and 3).

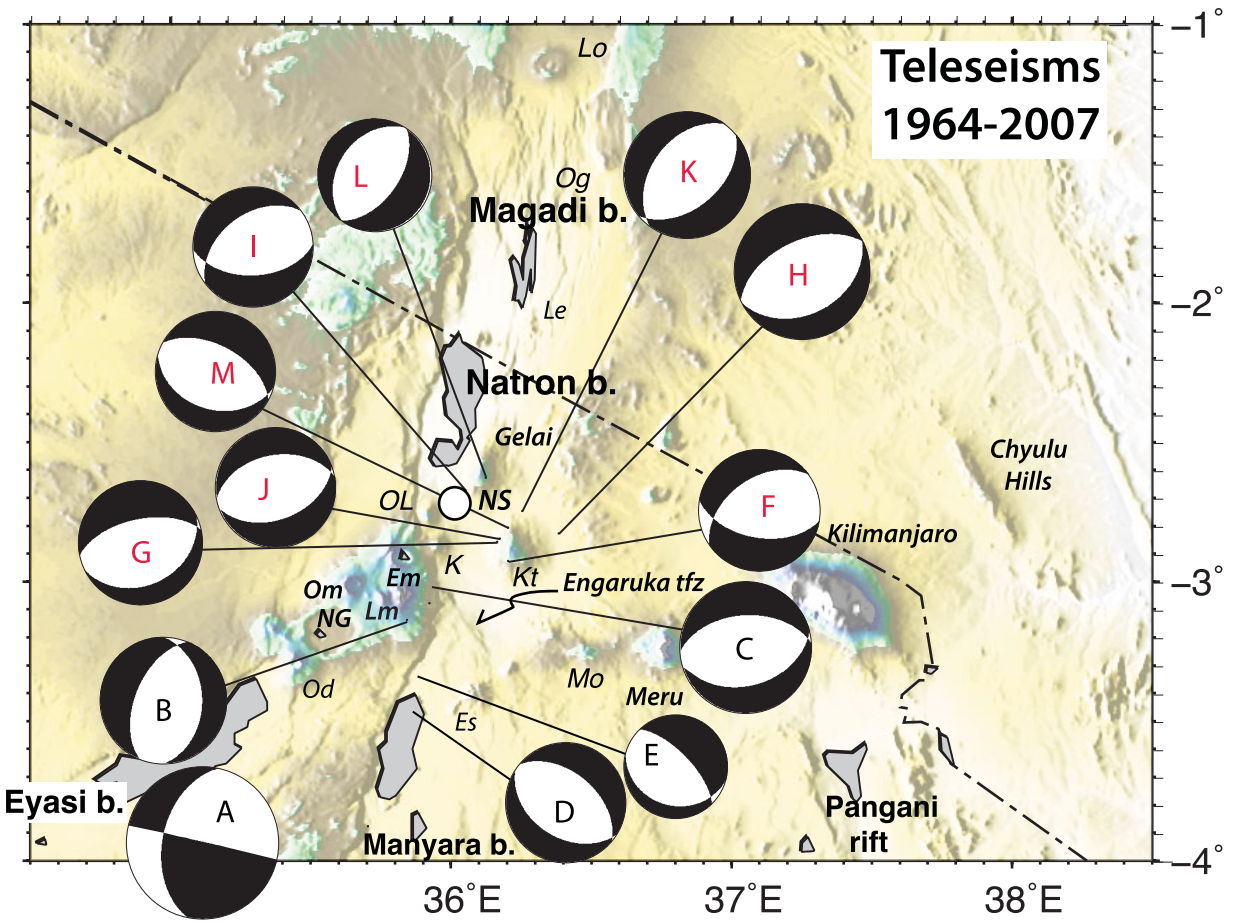

Figure 3. Mechanisms and locations of prior largest earthquakes in the North Tanzania Divergence since 1964 from *Engdahl et al.*, [1988]; *Nyblade and Langston* [1995], *Foster and Jackson* [1998], *Brazier et al.* [2005], *Yang and Chen* [2010], and *Craig et al.* [2011], as compiled by *Craig et al* [2011] (supporting information Table S1). Letters refer to sequential listing in supporting information Table S1. Red labels: 2007 seismovolcanic crisis. Note that location errors are 10 km or more, restricting direct comparisons with events in Figure 7. Volcanoes (from north to south) are Lo = Longonot; Og = Olorgesailie; Le = Lenderut; Gelai; NS = Naibor Soito monogenetic cone complex and xenolith field; Oldoinyo Lengai (carbonatite); K = Kerimasi (carbonatite); Kt = Kitumbeine; Em = Embagai; Om = Olmoti; Lm = Loolmalasin; NG = Ngorongoro; Od = Oldeani; Es = Essimingor; Mo = Monduli; Meru [after *Baker*, 1986; *Foster et al.*, 1997; *Mana et al.*, 2015].

Although the upper crustal contact between Archaean and Late Proterozoic crust lies west of the Magadi-Natron-Manyara rift zone, mantle xenolith data indicate that Archaean lithosphere underlies much of this rift sector [*Aulbach et al*., 2008, 2011], and that it has been metasomatized [e.g., *Chesley et al*., 1999; *Mattsson et al*., 2013; *Mana et al*., 2015] (Figure 2). Some of these magmatic and aqueous fluids may be sourced from the deep mantle, based on interpretations of geochemical and seismic data [e.g., *Pik et al*., 2006; *Julià and Nyblade*, 2013; *Thompson et al*., 2015].

The distribution and geochemistry of eruptive centers provides insights into magma and volatile migration through the plate, and its relation to crustal strain. The Magadi-Natron-Manyara area includes a large number of $<$7 Myr-old basaltic shields and composite cones that have a wide range of lava compositions including melilitites, basalts, nephelinites, phonolites, as well as carbonatites [e.g., *Dawson*, 1992; *Mollel et al*., 2008, 2011; *Mattsson and Tripoli*, 2011; *Mattsson et al*., 2013; *Mana et al*., 2015] (Figure 1 and supporting information Figure SM2). The three most important to our study are the carbonatitic Oldoinyo Lengai volcano, the monogenetic cone field of melilititic maars and nephelinitic cinder cones, and the 1 Myr-old Gelai volcano (Figure 1 and supporting information Figure SM2). Although *Dawson* [1992], *Mattsson and Tripoli* [2011], and *Mattsson et al*. [2013] called this cone field the "Lake Natron-Engaruka monogenetic field," we adopt the Maasai place name of Naibor Soito monogenetic field to avoid confusion with the Engaruka transfer fault and Natron basin. A unique geochemical signature in the lavas is the high CO_2 content of melilitites and carbonatites, probably derived from small partial melting of a metasomatized mantle source [*Fischer et al*., 2009; *Mattsson et al*., 2013; *Mana et al*., 2015]. The magmatic CO_2 degassing occurs not only at the active Oldoinyo Lengai volcano, but along faults bounding the Natron and Magadi basins, suggesting that the faults are conduits for gas transfer from the mantle to the atmosphere [*Lee et al*., 2016].

The Magadi, Natron, and Manyara rift basins are all half-graben bounded on their western margins by steep border faults that dip $\sim$60° at the surface [*Foster et al*., 1997; *Ring et al*., 2005; *Le Gall et al*., 2008; *Muirhead et al*., 2015]. They show a north to south younging pattern, but magmatism shows more complex trends [*Mana et al*., 2015]. The Crater Highlands is the fault-bounded crustal block between the Olduvai basin to the west, and the Natron-Manyara border faults, and it comprises many of the alkaline and composite volcanoes (Figure 1 and supporting information Figure SM2). Owing to their diachroneity, we briefly summarize rift evolution and crustal contraints basin by basin.

The northern Magadi basin is partially filled with $\leq$7 Myr-old trachytes and phonolites from volcanic complexes on the eastern side of the basin. At about 2 Ma, silicic and carbonatitic volcanoes started to form within the central rift valley (Figure 1 and supporting information Figure SM1). Revised ^{40}Ar-^{39}Ar dating of the stratigraphically highest volcanic units reveal that volcanism largely ceased by about 0.95 Ma [*Muirhead et al*., 2016]. Since this time, lavas covering the central basin floor were cut by many closely spaced faults [*Baker*, 1986; *Muirhead et al*., 2016]. Seismic refraction/wide-angle reflection, tomography, MT, and gravity data along the Kenya Rift International Seismic Project-94 (KRISP94) profile reveal a few kilometers of crustal thinning and evidence for 5+ km of magmatic underplate beneath the Magadi basin [*Birt et al*., 1997; *Thybo et al*., 2000; *Sippel et al*., 2017]. A narrow zone of thinned mantle lithosphere is interpreted directly beneath the fault-bounded rift basin: $\sim$90 km thick versus $>$125 km outside the rift zone [*Green et al*., 1991; *Ritsema et al*., 1999].

The original Natron basin, which contains lavas and sedimentary strata data at $\sim$3 Ma, was bounded by the Oldonyo Ogol fault [*Manega*, 1993; *Foster et al*., 1997; *McHenry et al*., 2011] (Figure 1). In the past 1.2–1 Myr the Songo border fault developed within this older basin to connect the Nguruman and Manyara border faults in a more direct line [*Foster et al*., 1997; *Muirhead et al*., 2016] (Figure 1). By 1.23 Ma, eruptive centers started to form within the basin bounded by the Songo fault and the monocline on its eastern side [*Dawson*, 1992; *Mana et al*., 2015; *Muirhead et al*., 2015, 2016]. Based on receiver function results, crust thins from $\sim$40 km on the margins to less than 30 km beneath the basin, with Vp/Vs ratios $>$1.85 beneath the Crater Highlands and southern Natron basin, as compared to $<$1.74 beneath the rift flanks [*Plasman et al*., 2017; *Roecker et al*., 2017].

A sub-E-W trending volcanic chain forms the northern margin of the Manyara basin, and it represents a broadly distributed transfer fault zone linking the Natron extensional basin to the Pangani rift zone to the east [*Foster et al*., 1997; *Muirhead et al*., 2015; *Delcamp et al*., 2016] (Figure 1). Although magmatism started between 6 and 4.7 Ma along the flanks of the Manyara basin [*Mollel et al*., 2008], the present morphology

developed after the widespread outpouring of largely basaltic lavas at 1 Ma [*Foster et al*., 1997]. Crustal tomography results indicate low-velocity zones beneath the Manyara basin and the sub-E-W trending volcanic lineament between Essimingor and Kilimanjaro [*Albaric et al*., 2014].

3. Data

The CRAFTI-CoLiBrEA network consisted of 39 broadband, three-component seismic stations installed between 12 January 2013 and 6 December 2014 (Figure 2). The network comprised Streckeisen STS-2, Guralp 3T and 40T, Trillium 120 with Reftek dataloggers from IRIS-PASSCAL, as well as two University of Rochester Nanometrics Compact sensors. All data were acquired at 50 Hz. Along with CRAFTI-CoLiBrEA data, we use data from GEOFON stations KIBK and KMBO in Kenya [*GEOFON Data Centre*, 1993] (Figure 4). After about a month's recording, Garmin GPS clocks used for timing began to fail, and by late June, all but 5 GPS units were nonfunctional. The catastrophic GPS failures remain unexplained. Robust clocks were installed in late November 2013. Owing to these issues, we analyze about 13 months of data (18 January to 12 February 2013, and 1 December 2013 to 1 December 2014). We relocate earthquakes from a swarm that includes m_b

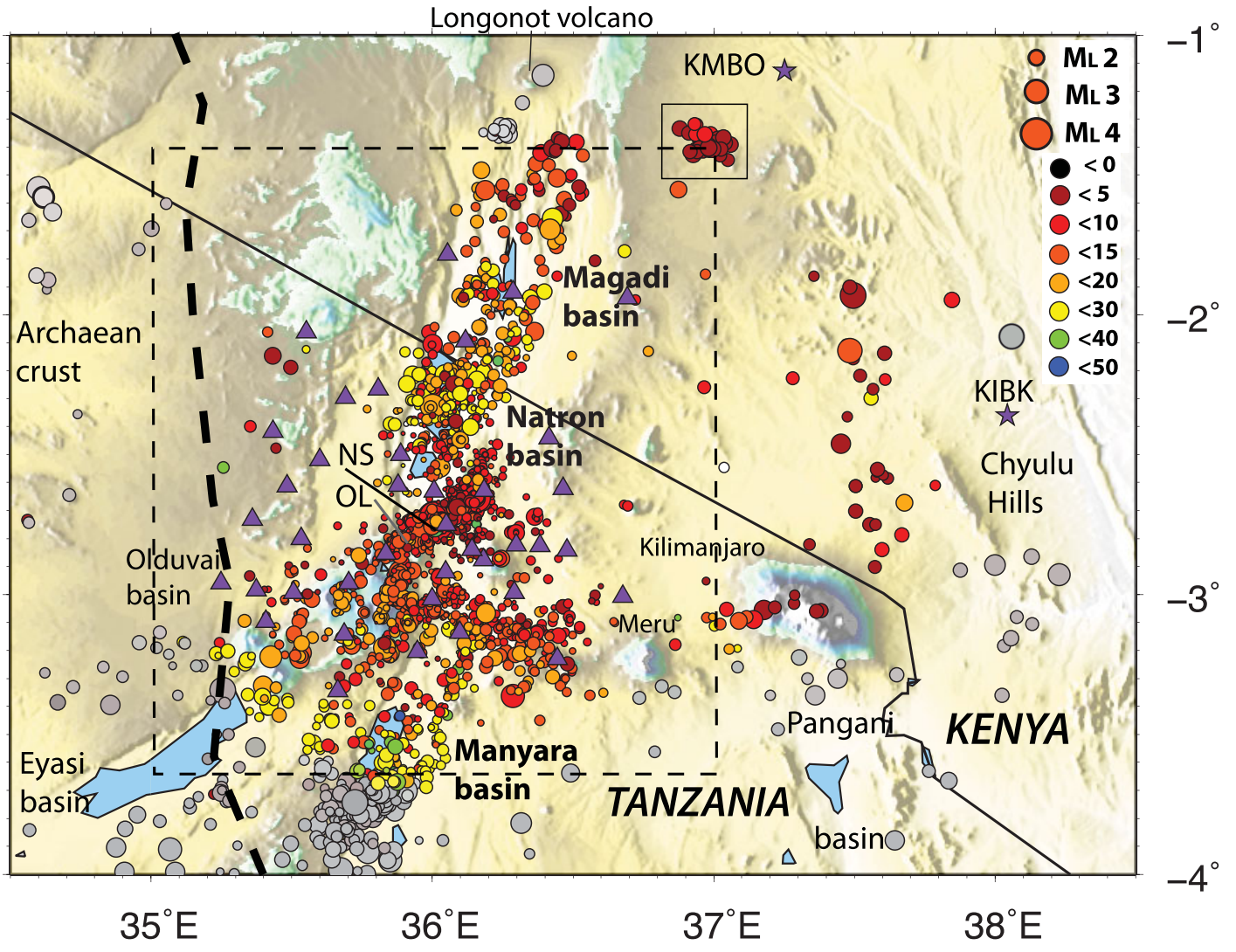

Figure 4. CRAFTI-CoLiBrEA earthquake locations determined from the absolute location algorithm Hypoinverse and using the 1-D velocity model of *Albaric et al*. [2010]. Bold dashed line is the surface contact of Archaean and Pan-African crust after *Manya and Maboko* [2003]. Events are color coded according to depth, and scaled to local magnitude, M_L. Events outside the array lacking depth constraints are scaled to magnitude and shaded gray. Purple triangles are seismometer locations. Purple stars are permanent GEOFON stations KMBO and KIBK; data from these stations were used in this study. Rectangle encloses Magadi-Natron-Manyara focus area indicated in Figures 2, 6, and 7. Small box south of KMBO indicates area of supporting information Figure S8, which compares earthquake locations and quarries.

Table 1. Focal Mechanisms Solutions, Classified as Group A, With up to 10 Solutions and 2σ of the Strike, Dip, and Rake, are All $\leq 10°$[a]

	Date			Time					Depth	Focal Mechanism							
	yyyy	mm	dd	hh	mm	ss.ss	Lon (°)	Lat (°)	(km)	Strike	Dip	Rake	M_L	# Sol	$2\sigma_{strike}$	# Picks	Ev #
Natron-Magadi	**2013**	**01**	**25**	**02**	**22**	**25.16**	**36.0987**	**−2.2227**	**19.0**	**19.6**	**55.6**	**−77.8**	**2.1**	**2**	**3.9**	**26**	**6**
	2014	**04**	**13**	**00**	**20**	**04.38**	**36.0657**	**−2.2963**	**22.5**	**200.4**	**26.8**	**−67.3**	**1.0**	**3**	**8.8**	**15**	**8**
	2014	**06**	**08**	**02**	**19**	**46.87**	**36.0088**	**−2.3727**	**21.0**	**172.4**	**18.0**	**−55.7**	**1.2**	**1**	**0.0**	**18**	**10**
	2014	**06**	**11**	**22**	**45**	**28.13**	**36.0410**	**−2.3182**	**19.4**	**265.7**	**44.0**	**−60.5**	**1.1**	**1**	**0.0**	**16**	**9**
	2014	**06**	**26**	**20**	**01**	**25.62**	**35.9273**	**−2.3075**	**24.3**	**185.2**	**26.8**	**−67.3**	**1.2**	**1**	**0.0**	**18**	**5**
	2014	**07**	**08**	**04**	**05**	**14.13**	**36.2162**	**−1.8407**	**22.7**	**325.0**	**5.0**	**−90.0**	**1.6**	**1**	**0.0**	**14**	**1**
	2014	**07**	**08**	**19**	**54**	**42.97**	**36.1080**	**−1.9495**	**15.5**	**175.7**	**18.0**	**33.0**	**1.6**	**2**	**0.0**	**14**	**2**
	2014	**07**	**22**	**07**	**38**	**14.10**	**35.9555**	**−2.4677**	**20.6**	**205.3**	**35.5**	**−54.0**	**1.8**	**1**	**0.0**	**24**	**11**
	2014	**08**	**17**	**12**	**21**	**22.93**	**35.9107**	**−2.2487**	**24.3**	**150.4**	**85.0**	**−85.0**	**2.1**	**2**	**5.0**	**19**	**4**
	2014	**08**	**25**	**22**	**37**	**45.61**	**36.0848**	**−2.2532**	**19.7**	**177.9**	**60.1**	**−84.2**	**1.4**	**1**	**0.0**	**19**	**7**
	2014	**11**	**01**	**00**	**48**	**34.36**	**36.1902**	**−1.9275**	**17.1**	**45.8**	**75.2**	**−79.7**	**2.6**	**1**	**0.0**	**18**	**3**
OL-NS-Gelai	**2013**	**06**	**03**	**03**	**24**	**44.51**	**36.0075**	**−2.7280**	**6.2**	**65.2**	**55.6**	**−77.8**	**4.3**	**2**	**1.4**	**18**	**13**
	2013	**06**	**03**	**09**	**53**	**10.51**	**36.0157**	**−2.7283**	**9.5**	**65.2**	**55.6**	**−77.8**	**4.4**	**2**	**1.4**	**13**	**14**
	2014	**01**	**29**	**02**	**47**	**17.43**	**36.1872**	**−2.6603**	**7.3**	**252.1**	**35.3**	**−81.3**	**1.4**	**4**	**6.2**	**17**	**19**
	2014	**03**	**24**	**07**	**38**	**23.51**	**35.9955**	**−2.7512**	**14.0**	**249.8**	**44.0**	**−60.5**	**2.1**	**3**	**1.5**	**20**	**31**
	2014	**04**	**18**	**09**	**52**	**16.09**	**35.9885**	**−2.8110**	**9.1**	**169.4**	**65.4**	**−79.0**	**1.3**	**4**	**7.7**	**12**	**33**
	2014	**05**	**02**	**00**	**51**	**04.87**	**35.9850**	**−2.8185**	**9.9**	**14.2**	**31.5**	**−70.6**	**1.2**	**1**	**0.0**	**14**	**32**
	2014	**06**	**05**	**17**	**50**	**51.48**	**36.0285**	**−2.7442**	**17.5**	**255.0**	**50.0**	**−90.0**	**1.9**	**6**	**10.0**	**20**	**26**
	2014	**06**	**05**	**17**	**51**	**45.46**	**36.0287**	**−2.7442**	**17.3**	**90.1**	**52.8**	**−64.6**	**2.6**	**3**	**6.0**	**26**	**25**
	2014	**06**	**07**	**19**	**33**	**55.90**	**36.0332**	**−2.7472**	**9.7**	**269.2**	**50.2**	**−83.5**	**2.8**	**3**	**5.0**	**23**	**27**
	2014	**06**	**13**	**04**	**03**	**18.00**	**36.1292**	**−2.6972**	**8.9**	**186.9**	**55.6**	**−77.8**	**1.4**	**1**	**0.0**	**16**	**20**
	2014	**06**	**29**	**01**	**49**	**26.22**	**36.1088**	**−2.6682**	**6.0**	**252.3**	**65.1**	**−84.5**	**2.2**	**3**	**9.4**	**31**	**16**
	2014	**06**	**30**	**06**	**13**	**19.34**	**35.9738**	**−2.7247**	**9.2**	**245.0**	**20.0**	**−90.0**	**2.3**	**1**	**0.0**	**26**	**21**
	2014	**07**	**21**	**19**	**58**	**37.69**	**36.0172**	**−2.7605**	**14.7**	**114.2**	**60.2**	**54.8**	**1.1**	**1**	**0.0**	**18**	**29**
	2014	**08**	**05**	**06**	**15**	**04.17**	**36.0143**	**−2.7278**	**15.9**	**95.7**	**55.6**	**−77.8**	**1.6**	**3**	**4.8**	**13**	**23**
	2014	**08**	**21**	**22**	**09**	**14.15**	**36.0720**	**−2.6858**	**9.1**	**232.9**	**44.8**	**−44.8**	**1.4**	**2**	**5.8**	**19**	**15**
	2014	**09**	**08**	**05**	**45**	**50.24**	**36.0123**	**−2.7183**	**9.4**	**58.0**	**45.9**	**−76.0**	**2.4**	**1**	**0.0**	**21**	**22**
	2014	**09**	**11**	**07**	**45**	**56.31**	**36.0323**	**−2.7277**	**10.0**	**202.0**	**58.7**	**−60.4**	**1.7**	**5**	**6.3**	**19**	**24**
	2014	**09**	**22**	**13**	**34**	**54.78**	**36.0013**	**−2.5740**	**14.4**	**47.3**	**65.1**	**−84.5**	**1.7**	**1**	**0.0**	**16**	**12**
	2014	**09**	**23**	**22**	**15**	**36.76**	**36.0222**	**−2.7488**	**9.6**	**197.4**	**51.6**	**−70.7**	**2.9**	**1**	**0.0**	**24**	**30**
	2014	**09**	**29**	**00**	**00**	**22.60**	**36.1628**	**−2.6550**	**6.0**	**330.0**	**25.0**	**−90.0**	**1.4**	**1**	**0.0**	**14**	**18**
	2014	**10**	**27**	**22**	**34**	**06.40**	**36.1318**	**−2.6640**	**8.6**	**303.6**	**30.4**	**−80.1**	**2.1**	**1**	**0.0**	**27**	**17**
Manyara	2013	02	05	04	51	02.57	36.2455	−2.8720	11.3	310.6	36.2	−72.9	2.1	1	0.0	22	28
	2014	02	18	17	17	06.27	35.5407	−3.0700	12.2	46.3	50.7	−77.0	1.4	1	0.0	14	35
	2014	04	19	18	42	23.23	35.8353	−3.2017	11.4	226.0	37.7	−65.0	1.6	1	0.0	19	38
	2014	06	29	08	28	24.11	35.9242	−3.0282	14.2	355.0	45.2	−83.0	2.0	3	1.8	24	37
	2014	07	06	21	07	22.44	36.3705	−3.1383	7.6	158.9	52.8	−64.6	1.8	2	1.8	18	39
	2014	07	20	23	36	02.24	35.8283	−2.8613	10.7	260.0	50.0	−90.0	1.3	1	0.0	23	34
	2014	07	22	17	55	05.58	35.8225	−3.6010	23.2	355.0	85.0	−90.0	2.1	1	0.0	19	40
	2014	09	15	12	36	20.62	35.5088	−3.1410	13.4	20.4	85.0	−85.0	2.0	1	0.0	17	36

[a]Focal mechanisms are plotted in Figure. 7. They are grouped with respect to region, as discussed in text and shown in Figure 8. Events in bold are included in the rose diagram (Figure 8) and Kostrov summation (supporting information Figure S10).

4.5 and m_b 4.6 earthquakes (as determined by NEIC) in June 2013 using only those stations with reliable GPS times (PR31, LN15, LN25, LN34, LN35, NG54, LL23; Figure 2). Noise levels were generally very low on stations placed in traditional grazing lands and national parks.

We also use a catalogue of earthquake focal mechanisms ($M_W > 4.5$) determined from waveform analyses of the largest earthquakes that were recorded in the area from 1964 to 2007, as summarized in Table 1 and Figure 3. These previous earthquakes provide the regional framework for our interpretation of the CRAFTI-CoLiBrEA network data.

4. Methods

4.1. Locations

P wave arrivals were hand-picked on Butterworth-filtered (1–2 Hz) vertical components of the 39 CRAFTI-CoLiBrEA stations and KIBK and KMBO using the Seismic Handler motif package [*Stammler*, 1993]. For each earthquake, the initial *P* wave picks were used to obtain an initial location, and horizontal components were then rotated to radial and transverse components. The S-phase was picked on the transverse component, and events located using Hypoinverse to produce a database of 3427 events. The database includes 40,754 *P* wave phases and 36,459 *S* wave phases. A minimum of six arrival time measurements with at least three

P arrivals was required to assign a location, but most events far surpassed this threshold with 20 or more picked arrival times. Absolute locations were determined using the Hypoinverse algorithm [*Klein*, 2002] and the 1-D velocity model of *Albaric et al*. [2010], which was used as the starting model in the crustal tomography [*Roecker et al*., 2017]. We used the Vp/Vs ratio of 1.74 determined from regression of *S*-*P* arrival times against *P* arrival times of earthquakes located within the network, but note that the final Vp/Vs starting model used in *Roecker et al*. [2017] is even lower at 1.72. The difference in earthquake locations is inconsequential.

Earthquakes ($N = 1253$) with good spatial coverage and recorded on 12 or more stations were relocated using the 3-D velocity model derived from joint inversion of ambient noise, our *P* and *S* arrival times, and Bouguer gravity data [*Roecker et al*., 2017] (supporting information Figures SM3 and SM4). The June 2013 swarm was not included owing to the small number of stations with reliable timing. Only this subset of 1253 events was relocated using the 3-D velocity model because the wave speed modeling utilizes those hypocenters that have the most relevant information to the wave speed inverse problem and does not generate a comprehensive catalogue. We also used the double-difference relative relocation analyses to study the spatial relation of nearby earthquakes [*Waldhauser and Ellsworth*, 2000]. We use cross-correlated waveforms to improve *P* wave picks, and hypoDD V2.1beta that allows for variations in the elevations of stations and station-dependent velocity variations, in our application. Where the separation between hypocenters is small in comparison to event-to-station distances and to the scale of velocity variations, the ray paths from source to stations are similar, and the differences in travel times for the events provide a measure of their spatial separation [*Waldhauser and Ellsworth*, 2000]. The HypoDD algorithm adjusts the vector difference between nearby hypocentral pairs and updates locations through successive iterations, and allows for user defined weighting of phase picks and cross-correlated *P* wave picks.

4.2. Magnitudes

Given the presence of magma bodies as well as cratonic lithosphere within the study area, attenuation may vary spatially. After removing individual instrument responses and convolving with the nominal Wood-Anderson instrument response, [e.g., *Richter*, 1958] we measured the peak amplitudes for ~73,000 N and E waveforms. Following the method of *Keir et al*. [2006b], we used the amplitudes in a linear inversion for local station corrections, individual local earthquake magnitudes (M_L), and two linear distance correction factors (supporting information Figure SM5). We compute the magnitude at each station for both horizontal components, and then use the average of these values as the overall earthquake magnitude. There is no bias introduced, in comparison to standard methods of using the larger of the two horizontal amplitudes, because we have determined the N-S and E-W station corrections. The revised local magnitude scaling relationship with station corrections compensates for locally high seismic signal attenuation (see supporting information Figure SM6).

4.3. Focal Mechanisms

We use the first-motion modeling program FOCMEC, which assumes a double-couple solution to analyze earthquakes with $M \geq 1$ with azimuthal gap in station coverage less than 127° [*Snoke et al*., 1984]. The take-off angle and backazimuth from the Hypoinverse solution and polarity of the vertical waveform are used in the grid search algorithm for best fitting nodal planes, and P and T axes (supporting information Figure SM7).

5. Results

5.1. Absolute Locations: 1-D Velocity Model

Most of the 3427 earthquakes were tectonic events with impulsive *P* arrivals, and clear *S* arrivals at most stations. Location uncertainties for earthquakes within our array have mean horizontal uncertainty of 1.2 km, and mean depth uncertainty of 1.8 km.

Although earthquakes outside the array have poorly determined or indeterminate depths and location uncertainties up to 10 km, they demonstrate active deformation within the Tanzania craton and the numerous volcanic lineaments (Figure 4). The Eyasi rift and uplifted flanks are seismically active, as are some topographic scarps in Archaean crust (Figures 1 and 4). We also detected persistent earthquakes in the southern Manyara basin (Figure 4). Earthquake activity levels in the south Manyara basin have been high since first

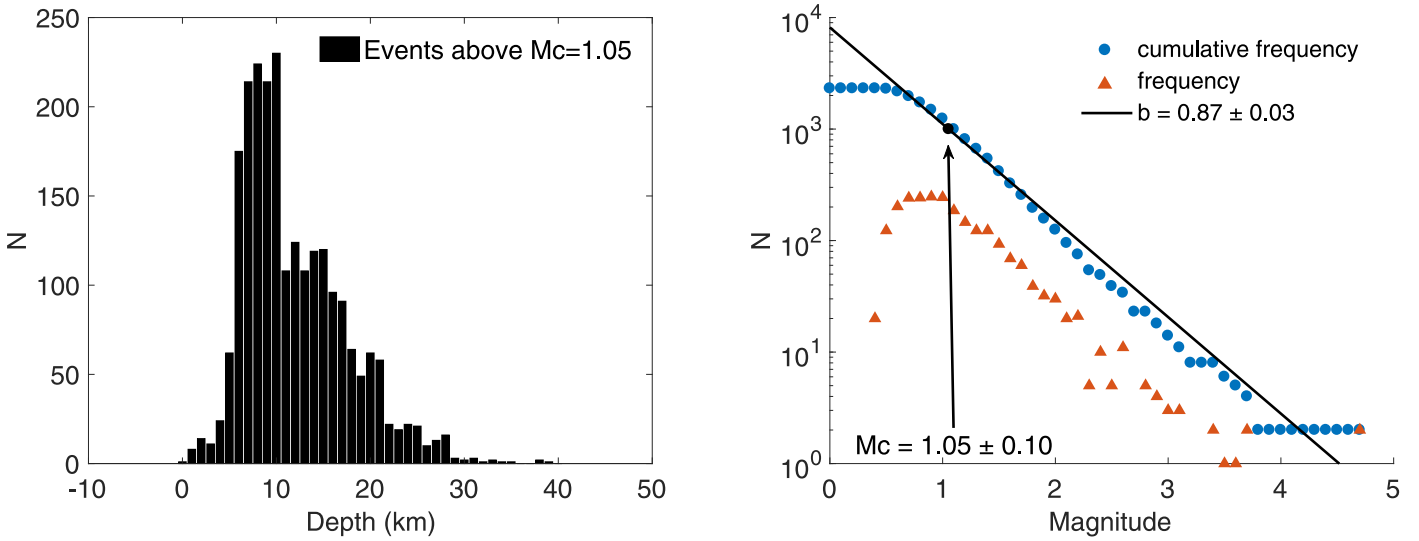

Figure 5. (a) The depth distribution of earthquakes *N* for events within the CRAFTI-CoLiBrEA array with well-determined depths. (b) (right) After determining a magnitude of completeness, *Mc*, using the adjusted maximum curvature method of *Woessner and Wiemer* [2005], the *b*-value estimate of 0.87 ± 0.03 was determined via the maximum likelihood method.

monitored in 1992 [*Birt et al*., 1997; *Mulibo and Nyblade*, 2009], and studied in detail with an array in 2007–2008 [*Albaric et al*., 2010, 2014]. Earthquakes occurred beneath the Kilimanjaro edifice, and along the NW-oriented line of 1.4 Ma-Holocene eruptive centers and fissural vents referred to as the Chyulu hills (∼36°E, 2.6° S), which may have a lower crustal magma chamber [*Novak et al*., 1997] (Figures 1 and 3). The events at about 37°E, 1.4°S are very shallow (≤5 km), are lower frequency, and are in an industrial area with multiple quarries; they may be blasts. As shown in supporting information Figure SM8, all are within 0.7–7 km of a quarry, providing a bound on location accuracy at the edge of the array. Only those earthquakes within or near the array are relocated and used in interpretations (sections 5.3–5.6).

5.2. Magnitudes

Local earthquake magnitudes range from 0.4 to 4.7 (Figure 5). Two of the earthquakes were detected teleseismically, and assigned body wave magnitudes by the NEIC, providing some calibration of our local magnitude scale. The 03:24 3 June 2013 m_b 4.5 and 09:53 m_b 4.6 earthquakes have local magnitudes of 4.7 ± 0.3 and 4.7 ± 0.4, respectively, showing agreement with the NEIC estimates. The errors are larger for this group of events owing to the small number of stations operational. Important to note is that the 03:24 earthquake was mislocated by approximately 26 km, and the 09:53 earthquake by approximately 5 km in the NEIC catalogue.

5.3. *b*-Value

The frequency distribution of earthquakes of any given magnitude follows a log linear relation:

$$\log N = a - bM_L$$

where M_L is local earthquake magnitude and *N* is the number of earthquakes of magnitude larger than the magnitude threshold [*Gutenberg and Richter*, 1944]. The largest magnitude earthquakes are rare, whereas small magnitude earthquakes are common. The slope of the curve, *b*, is inversely proportional to the differential stress [e.g., *Scholz*, 1968, 2015]. Although the period of earthquake observations is 1–4 orders of magnitude shorter than the period of tectonic and volcano-tectonic rifting cycles, strain released through small earthquakes, averaged on a regional scale, mimics tectonic deformation [e.g., *Amelung and King*, 1997; *Albaric et al*., 2010].

We use the maximum likelihood method [*Aki*, 1965; *Utsu*, 1965] to estimate *a*-value and *b*-value from the combined data set of well-located earthquakes within the array, and within the Oldoinyo Lengai-Naibor Soito-Gelai (OL-NS-G) volcanic line where seismicity is most intense (Figure 5). The magnitude of completeness, *Mc*, is $M_L = 1.05 \pm 0.10$ found using the maximum curvature method, and applying the +0.2 correction factor of *Woessner and Wiemer* [2005]. The uncertainty is reported using the bootstrap method, which

takes into account uncertainty of the *b*-value fit, as well as uncertainties in *Mc*, since the latter affects the former [*Woessner and Wiemer*, 2005]. The *b*-value for the entire data set ($N = 2315$) is 0.87 ± 0.03 (Figure 5 and supporting information Table SM2). We also estimated *Mc*, *b*-value, and *a*-value in the OL-NS-G region which encompasses 51% of the data set, as well as the 2007 dike intrusion (supporting information Figure SM9). The *b*-value is 0.94 ± 0.05, which lies within the uncertainty of the entire region (supporting information Figure SM9 and supporting information Table SM2).

The *b*-value of 0.87 ± 0.03 estimated for the Magadi-Natron-Manyara rift zone is identical to the *b*-value of 0.87 for the central Kenya rift [*Tongue et al*., 1994], and similar to the *b*-value of 0.84 for Tanzania, which includes the Archaean craton [*Langston et al*., 1998], and 0.9 for the intensely intruded and faulted Danakil Depression [*Illsley-Kemp et al*., 2017] (supporting information Figure SM1). A large number of earthquakes occurred south of our array in the Manyara basin where *Albaric et al*. [2010] determine a *b*-value of 1.06, using local magnitudes estimated with a regional magnitude scaling [*Hollnack and Stangl*, 1998]. *Ibs-von Seht et al*. [2001] estimate an unusually low *b*-value of 0.77 for a 7 month time period of observation in the Magadi basin, which included an intense swarm interpreted as a dike intrusion. Inclusion of events from the 1989 Magadi swarm may explain the apparent temporal variations between the two studies, as has been observed in other magmatically active zones [e.g., *Wiemer et al*., 1998; *Illsley-Kemp et al*., 2017].

5.4. Double-Difference Locations

The data set was too large to relocate in one step, so the region was subdivided into six areas where similarities in earthquake sources are expected: Magadi basin; Natron basin; Embagai-OL-NS-G chain; Crater Highlands; Engaruka transfer fault zone; and northern Manyara basin (Figure 1). Band-pass-filtered (1.5–15 Hz) waveforms with a 0.2–0.3 s time window centered on the *P* arrival were cross correlated using the GISMO suite [*Reyes and West*, 2011]. Event pairs with a correlation coefficient ≥ 0.5 were used in the double-difference relocation algorithm. The number of event pairs varied widely between regions, with the fewest event pairs (110) in the Magadi basin region where *P* wave arrival cross correlations were complicated by scattered and reflected wave arrivals immediately after the *P* arrival, and where station coverage was sparse. The largest number of event pairs was in the Naibor Soito-Gelai area where repeating earthquakes with highly correlated waveforms occurred, as outlined in a complementary study [*Oliva et al*., 2017]. The cross-correlated times were given a progressively higher weighting than the manual pick times in the later iterations.

We included topography and used station-specific 1-D velocity models extracted from the results of *Roecker et al*. [2017]. In the Naibor Soito subregion, the relocated events diverged during iterative double-differencing. This zone encloses Oldoinyo Lengai and Gelai volcanoes, and is underlain by a lower crustal low-velocity zone [*Roecker et al*., 2017]. Solutions converged after the amplitude of the velocity reduction was reduced, suggesting that divergence was caused by inadequate ray-tracing through the low-velocity zones in the middle and lower crust. The reduced depth range of the low-velocity zone in the area near Oldoinyo Lengai and Gelai volcanoes leads to ≤ 1 km upward shifts in the centroids of the double-difference clusters relative to the 3-D locations, in a sense consistent with the lower velocities in the 3-D model (supporting information Figure SM4).

Mean location uncertainties determined from singular value decomposition analyses for the Magadi basin are 2.18 km in horizontal position and 3.64 km in depth, consistent with location errors in this area found using Hypoinverse. At the southern end of our array, Manyara basin relocation uncertainties are 1.62 km in horizontal location and 3.63 km in depth. Locations in the Crater Highlands and central Natron regions have uncertainties of 1.07 km in horizontal position and 0.70 km in depth. The large number of earthquakes in the Naibor Soito region, which encompasses Oldoinyo Lengai volcano and Gelai volcano have the smallest mean uncertainties: horizontal errors of ± 0.09 km and depth errors of ± 0.19 km.

Systematic comparisons of results from each relocation method are complicated because different subsets of earthquakes were considered, and because Hypoinverse assumes a flat surface, whereas hypoDD and the 3-D model consider topography (Figure 6 and supporting information Figure SM3). The double-difference earthquakes are those with eight or more event pairs with *P* wave arrivals that are well correlated, whereas the events used in the tomography model were chosen to provide a regular spatial distribution to sample the model space, effectively reducing the effects of clustering. Histograms of depths, which have the largest uncertainties, provide a means to evaluate differences between the absolute and relocated

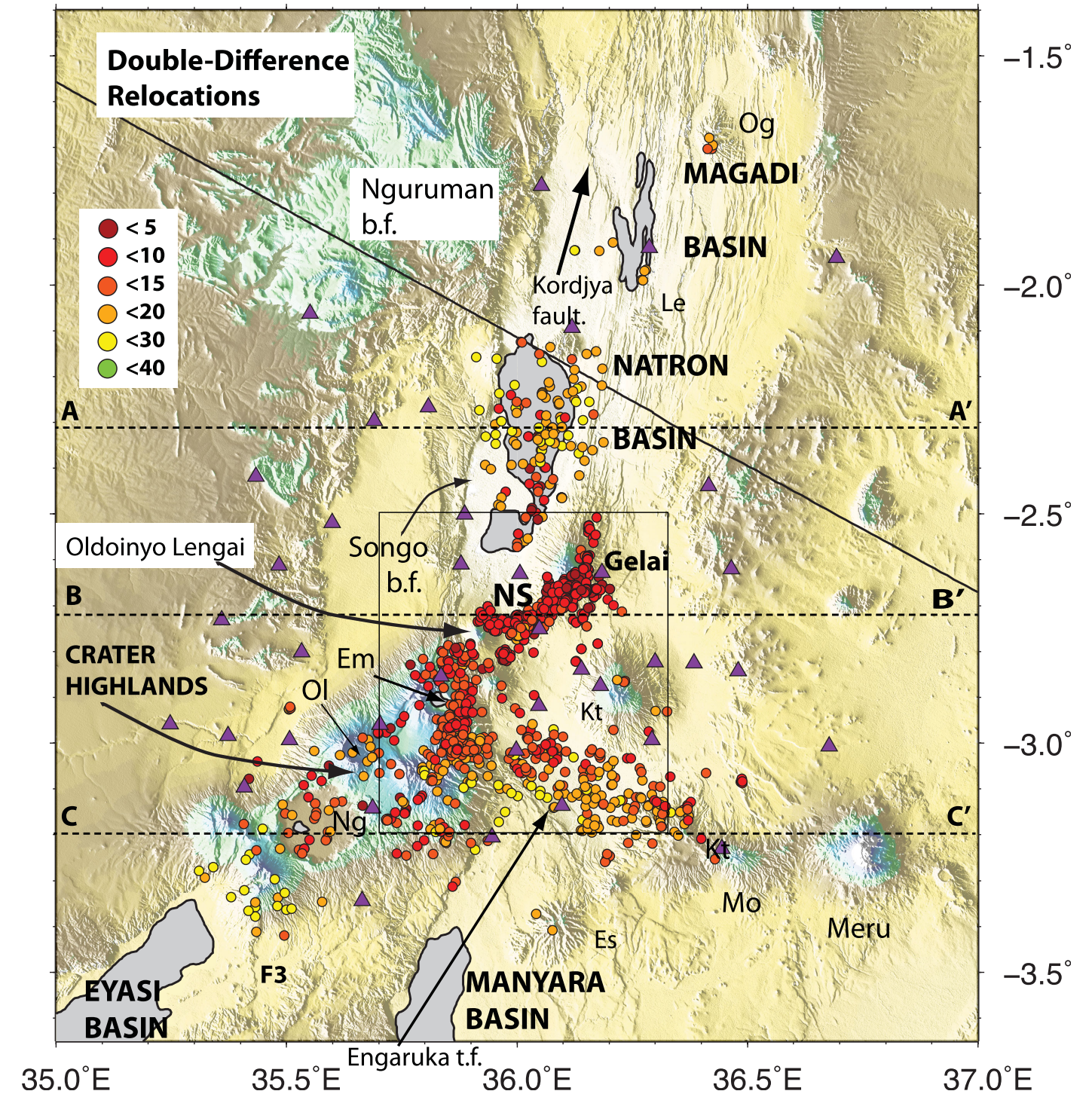

Figure 6. Earthquake locations from the double-difference analyses of catalogue times and *P* wave cross correlations, combined from smaller bins spanning the network. See text for details of catalogue and cross-correlation weightings. Epicenters are color coded with depth. Labels refer to volcanoes NS = Naibor Soito monogenetic cone field; Em = Embagai; Ol = Olmoti; Kt = Kitumbeine; Ng = Ngorongoro; Es = Essimingor; Mo = Monduli. F3 is an unnamed normal fault. Cross sections in Figure 9 are E-W profiles at 2.3°S (A–A′), 2.72°S (B–B′), and 3.2°S (C–C′). Epicentral locations in 10 km-wide swath centered on each line are projected onto the line of each cross section.

events (supporting information Figure SM4). The 3-D and double-difference hypocenter locations show no systematic depth differences. The events at depths >25 km in the absolute locations occurred in the northern Manyara basin, which was not imaged in the crustal tomography. The lower crustal earthquakes in the Manyara basin are consistent with depth distributions from the earlier work of *Albaric et al.* [2010, 2014].

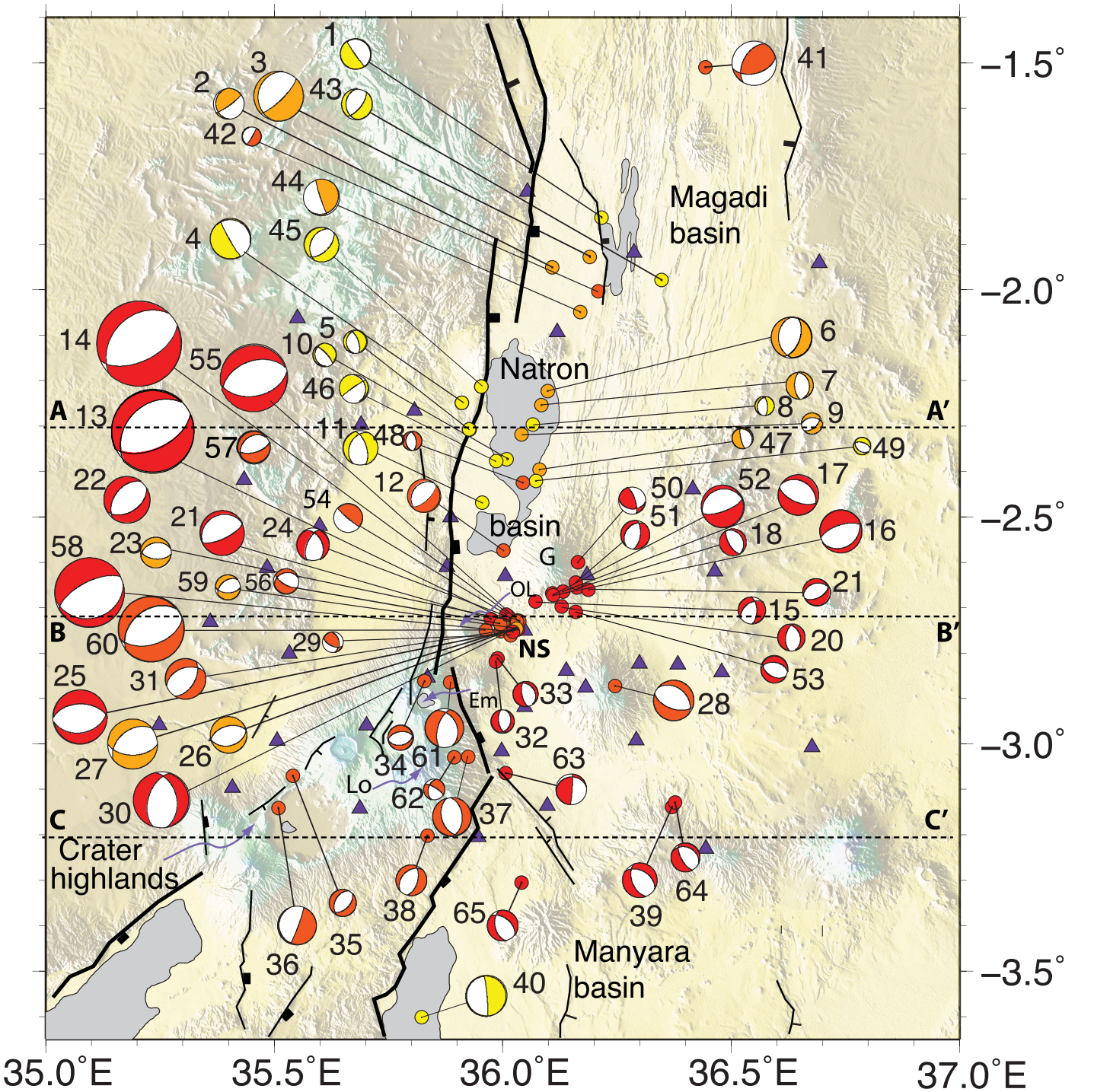

Figure 7. Focal mechanism solutions color coded with depth and scaled with magnitude determined from *P* wave first motions on the CRAFTI-CoLiBrEA array that included permanent stations KMBO and KIBK (Figure 2). Events 1–40 are listed in Table 1 and have nodal planes constrained to $2\sigma \leq 10°$, and Events 41–65 have nodal planes constrained to $2\sigma \leq 20°$, as in Table 2. Cross sections in Figure 9 are E-W profiles at 2.3°S (A–A′), 2.72°S (B–B′), and 3.2°S (C–C′). Focal mechanisms in 10 km-wide swath centered on each line are projected onto the line of each cross section.

5.5. Focal Mechanisms

Earthquakes with clear *P* arrivals on 8 or more stations and with azimuthal gaps $\leq$127° were screened for focal mechanism solutions. We use takeoff angles from the absolute locations for consistency. Events 13 and 14 are the two M_L 4.7 earthquakes that occurred during the time period of GPS failures, but we can still

Table 2. Focal Mechanism Solutions, Classified as Group B, With up to 10 Solutions and 2σ of the Strike, Dip, and Rake, are All $\leq 20°$[a]

	Date			Time					Depth	Focal Mechanism							
	yyyy	mm	dd	hh	mm	ss.ss	Lon (°)	Lat (°)	(km)	Strike	Dip	Rake	M_L	# Sol	$2\sigma_{strike}$	# Picks	Ev #
Natron-Magadi	**2014**	**01**	**29**	**15**	**28**	**54.98**	**35.9860**	**−2.3763**	**20.7**	**234.7**	**85.3**	**−69.9**	**1.5**	**6**	**7.2**	**18**	**46**
	2014	**02**	**28**	**13**	**08**	**02.60**	**36.3475**	**−1.9780**	**20.8**	**37.7**	**65.9**	**−73.5**	**1.6**	**6**	**12.5**	**10**	**43**
	2014	**03**	**12**	**16**	**52**	**56.48**	**36.1692**	**−2.0487**	**16.1**	**161.4**	**85.1**	**80.0**	**1.9**	**6**	**14.3**	**16**	**44**
	2014	**04**	**19**	**23**	**14**	**03.70**	**36.0730**	**−2.4202**	**20.5**	**128.0**	**36.2**	**−72.9**	**0.9**	**6**	**9.2**	**12**	**49**
	2014	**06**	**22**	**14**	**27**	**15.25**	**35.9528**	**−2.2128**	**21.1**	**45.0**	**55.6**	**−77.8**	**1.8**	**5**	**3.5**	**20**	**45**
	2014	**07**	**02**	**01**	**05**	**51.58**	**36.2090**	**−2.0030**	**11.4**	**30.4**	**85.0**	**−85.0**	**1.0**	**7**	**19.6**	**11**	**42**
	2014	**08**	**24**	**20**	**23**	**47.17**	**36.0807**	**−2.3960**	**19.2**	**167.4**	**75.2**	**−79.7**	**1.1**	**4**	**12.0**	**17**	**47**
	2014	**09**	**02**	**22**	**44**	**13.76**	**36.0440**	**−2.4247**	**12.3**	**182.1**	**35.3**	**−81.3**	**1.0**	**3**	**4.8**	**13**	**48**
	2014	09	09	01	07	22.18	36.4438	−1.5097	12.5	209.7	50.1	56.6	2.3	5	5.5	15	41
OL-NS-Gelai	**2013**	**01**	**27**	**05**	**55**	**32.77**	**36.1600**	**−2.7090**	**9.9**	**118.9**	**45.9**	**−76.0**	**1.4**	**3**	**5.0**	**15**	**53**
	2013	**01**	**27**	**20**	**25**	**22.34**	**35.9947**	**−2.7357**	**10.9**	**120.2**	**66.6**	**−68.1**	**1.3**	**7**	**7.3**	**19**	**56**
	2014	**03**	**16**	**11**	**53**	**58.30**	**36.1597**	**−2.6445**	**6.8**	**219.6**	**33.2**	**−61.8**	**1.5**	**5**	**4.9**	**16**	**51**
	2014	**05**	**10**	**21**	**02**	**22.46**	**36.1647**	**−2.5990**	**8.0**	**97.0**	**35.5**	**30.6**	**1.4**	**7**	**4.8**	**17**	**50**
	2014	**06**	**05**	**18**	**13**	**03.20**	**36.0302**	**−2.7455**	**16.9**	**90.1**	**52.8**	**−64.6**	**1.3**	**7**	**13.4**	**18**	**59**
	2014	**06**	**25**	**11**	**11**	**15.80**	**36.1102**	**−2.6720**	**6.8**	**250.0**	**20.0**	**−90.0**	**2.2**	**2**	**1.5**	**26**	**52**
	2014	**08**	**04**	**03**	**06**	**10.20**	**36.0223**	**−2.7523**	**9.8**	**75.6**	**25.5**	**−78.3**	**3.6**	**5**	**11.5**	**26**	**58**
	2014	**08**	**07**	**01**	**11**	**36.73**	**35.9627**	**−2.7492**	**10.1**	**71.7**	**50.7**	**−77.0**	**3.4**	**3**	**15.4**	**28**	**60**
	2014	**09**	**05**	**17**	**54**	**04.65**	**36.0080**	**−2.7148**	**9.8**	**80.0**	**45.2**	**−83.0**	**3.5**	**6**	**13.3**	**30**	**55**
	2014	**09**	**11**	**09**	**20**	**52.11**	**36.0313**	**−2.7295**	**10.1**	**74.2**	**60.5**	**−78.5**	**1.7**	**4**	**0.5**	**19**	**57**
	2014	**09**	**15**	**16**	**15**	**16.78**	**36.0363**	**−2.7290**	**11.6**	**265.1**	**7.1**	**44.9**	**1.5**	**6**	**12.1**	**13**	**54**
Manyara	2014	01	26	22	17	29.11	35.8942	−3.0285	11.4	194.7	44.0	−22.2	1.1	3	0.7	17	62
	2014	04	19	02	36	17.46	36.0407	−3.3057	8.8	167.1	48.4	−62.8	1.6	6	13.9	21	65
	2014	04	24	20	16	14.15	36.0063	−3.0640	9.9	3.6	85.3	69.9	1.6	4	0.8	15	63
	2014	07	06	00	51	18.08	36.3775	−3.1283	7.6	150.9	65.9	−73.5	1.5	3	5.3	13	64
	2014	09	12	17	55	24.68	35.8853	−2.8638	12.4	196.5	62.0	−67.2	2.0	8	1.1	26	61

[a]These are plotted in Figure. 7. They are grouped with respect to region, as discussed in text and shown in Figure 8. Events in bold are included in the rose diagram (Figure 8) and Kostrov summation (supporting information Figure S10).

use the *P* wave polarities and estimate takeoff angles using nearby events with accurate timing. Of the ~200 earthquakes considered, 40 had strike, dip, and rake of the better constrained slip plane with $2\sigma \leq 10°$ (class A, Table 1, Figure 7). Owing to the locally complex crustal velocity structure that adds uncertainty to takeoff angles from event relocations, we allowed up to two P-phase errors if within 5° of a nodal plane. An additional 26 events had strike, dip, and rake of the slip plane with $2\sigma \leq 20°$ (class B, Table 2, Figure 7). Patterns in the mechanisms emerge when they are considered in terms of along-axis segmentation, as outlined below.

5.6. Extension Direction

We test the hypothesis that a local rotation in extension direction occurs in the OL-NS-G region, and we group earthquake focal mechanisms into three zones: (1) the Magadi-Natron rift segments north of the chain; (2) the Oldoinyo Lengai-Naibor Soito-Gelai (OL-NS-G) magmatic chain; and (3) the northern Manyara rift segment, which includes parts of the Engaruka transfer fault and Essimingor-Kilimanjaro volcanic chain (Figure 8). Owing to the comparatively large (≥10 km) location errors of earthquakes prior to our array, we evaluate them separately from our precisely located events, and compare results.

Earthquake focal mechanisms from our temporary array, and the prior events in the region indicate a local rotation of the regional sub-E-W extension direction to NNW-SSE in the region between the northern Manyara basin and the southern Natron basin. Rose diagrams show the azimuthal distribution of extension directions (T axes) of the focal mechanisms regardless of magnitude. On the other hand, Kostrov summation of the focal mechanisms are weighted by seismic moment, and are therefore dominated by the largest earthquakes and are more relevant when assessing extension direction in light of seismic moment release [*Kostrov*, 1974; *Jackson and McKenzie*, 1988] (see supporting information section 6). The T axis directions determined from the summed moment tensors in the OL-NS-G magmatic chain (N148°E for the local earthquakes and N158°E for the prior catalog, supporting information Figure SM10 and supporting information Table SM3) are consistent with the extension direction indicated in rose diagrams of T axes orientations (N148°E ±17° and N160°E ± 14°, for the local and prior earthquakes, respectively, Figure 8). The few teleseisms in the weakly magmatic Manyara rift segment result in a wide spread in the rose diagram (mean vector, N51°E ± 43°, Figure 8), whereas a moment-weighted summation shows E-W extension (N92°E,

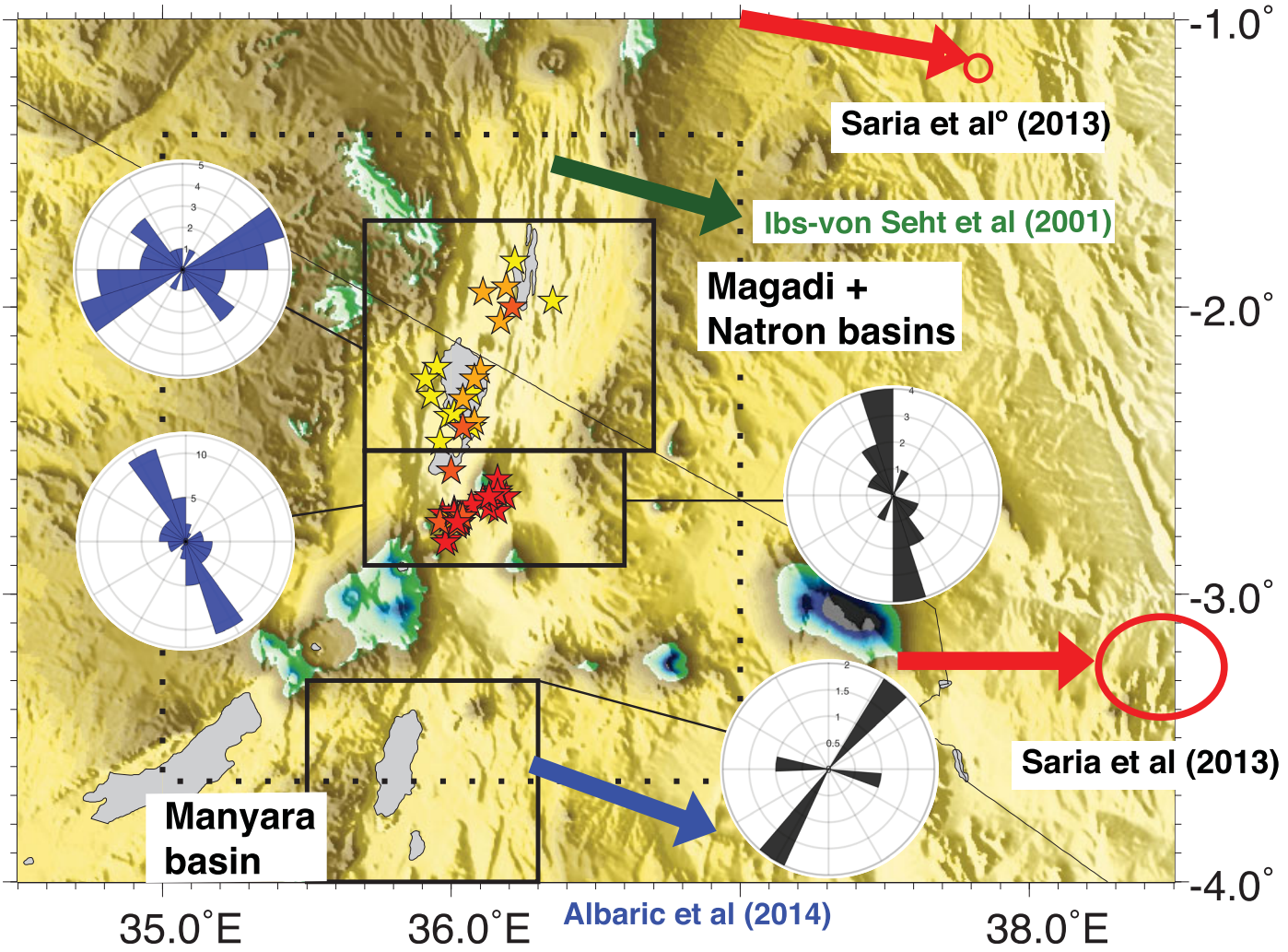

Figure 8. Rose diagrams of T axes from focal mechanisms in each of the three boxes chosen to isolate the Oldoinyo Lengai-Naibor Soito-Gelai volcanic chain where prior mechanisms (Figure 3) and our new data (Figure 7) suggest a stress field rotation from the Magadi and Natron basins to the north, and the Manyara basin to the south. Stars are the local events from Figure 7 that are included in each group. Our results are shown in blue, and compared to results using the mechanisms from prior studies of teleseismically and regionally detected earthquakes spanning 1964–2007 shown in black (from Figure 3 and supporting information Table S1). Red arrows with error ellipses are extension direction determined from geodetic data [*Saria et al.*, 2013]. Green arrow is the T axis (105 ± 5°) determined from a similar analyses of seismic data from the Magadi basin [*Ibs-von Seht et al.*, 2001], and blue arrow is the T axis direction (110°) from inversion of focal mechanism solutions in the Manyara area [*Albaric et al.*, 2014]. Dotted rectangle shows the extent of Figures 2, 6, and 7.

supporting information Figure SM10). The Magadi-Natron rose diagram indicates ENE-directed extension (N92°E ± 20°), a slight rotation from the Kostrov summation T axis (N122°E), the N106°E Magadi extension direction determined by *Ibs-von Seht et al.* [2001], and the geodetically determined opening to the east (N105°E) [*Saria et al.*, 2013] (Figure 8 and supporting information Figure SM10).

Earthquakes within the volcanic chain have an overall NNW-directed extension for both the CRAFTI-CoLiBrEA events, and the prior earthquakes, which are all from the 2007 diking episode (supporting information Table SM1). The two catalogs reveal a T axis clockwise rotation of 43°–55° from the upper bound on the geodetically determined regional extension direction of N90°E ± 15° [*Saria et al.*, 2013], as well as an 55°–70° and 40°–50° rotation from the Magadi-Natron opening direction from CRAFTI-CoLiBrEA (N92°E ± 20° T axis) and Manyara T axis direction (N110°E) of *Albaric et al.* [2014], respectively.

Our 13 month-long period of seismic recording is short compared to tectonic and magmatic rifting cycles, but the prior earthquakes span 44 years, providing a crude estimate of seismic strain rates (supporting information Table SM3). The largest strain rates occur in the magmatically active zone between the Natron and Manyara basins. Converting our strain rate estimates to extensional velocities, the maximum rate determined from events prior to our array is 0.11 mm yr^{-1} during the 2007 diking sequence, or about 30 times

smaller than the opening rate predicted by models of geodetic data [*Saria et al*., 2013]. Our observations of a long-term process are incomplete, but they clearly show a seismic strain deficit in comparison to these independent measures, suggesting that most of the plate opening occurs aseismically in this rift sector. The 2007–2008 seismovolcanic crisis in the Natron basin, therefore, may be representative of current deformation processes in this rift sector; magma intrusion and creep may contribute to the order of magnitude difference between the geodetic and seismic strain rates across this magmatic early-stage rift zone.

6. Discussion

Precise earthquake locations, and orientation of T axes of locally detected earthquakes and prior earthquakes detected regionally and teleseismically were integrated with results of receiver function [*Plasman et al*., 2017], crustal tomography [*Roecker et al*., 2017], spatial variations in time-averaged deformation from surficial structural studies [*Muirhead et al*., 2016; *Lee et al*., 2017], and gas chemistry measurements [*Lee et al*., 2016], to interpret the localization of strain and magmatism in this early-stage, magmatic rift zone (Figures 9 and 10). For ease of discussion, we refer to focal mechanisms by event number as listed in Table 1 and shown in Figure 7.

6.1. Along-Axis Segmentation and Kinematics

Magadi basin: Seismicity occurs throughout the depth range 4–25 km beneath the ~4 km deep Magadi basin, with the deepest events near projections of border faults, assuming surface dips [*Muirhead et al*., 2015]. Small magnitude earthquakes also occurred beneath Olorgesailie and Lenderut volcanoes (Figure 1, supporting information Figure SM2, and Figures 6 and 7). Exceptions are small magnitude, perhaps nontectonic Events 2 and 41 in the central Magadi basin, which are compressional (Figure 8). Our earthquake focal mechanisms indicate slip along NNW to NNE-striking, steep planes (Figure 7). Event 1 has a near vertical NNW-striking nodal plane that parallels the Kordjya fault (Figures 1 and 7), which releases magmatic CO_2 dissolved in alkaline springs [*Lee et al*., 2017] and through diffuse degassing [*Lee et al*., 2016; *Muirhead et al*., 2016].

The spatial distribution, depth extent, and focal mechanisms of our results are similar to those from an earlier seismic experiment in the central Magadi basin [*Ibs-von Seht et al*., 2001], which found high levels of activity within the central Magadi basin, as well as lower crustal (20–26 km) seismicity in some areas. An intense swarm of upward-migrating earthquakes occurred in 1998 beneath northern Lake Magadi, which *Ibs-von Seht et al*. [2001] interpreted as evidence for a dike intrusion. Focal mechanisms for the 1998 swarm are similar to one another, and they indicate a N106°E minimum compressive stress direction [*Ibs-von Seht et al*., 2001].

Receiver function results indicate that the crust thins from 35 km on the western flank to 29 km beneath the faulted basin, indicating 17% extension [*Plasman et al*., 2017]. This stretching estimate is identical with results of refraction-wide-angle reflection studies of *Birt et al*. [1997], assuming that the highly reflective, high velocity layer beneath the Magadi basin between 29 and 34 km is mafic underplate added to the crust during mechanical thinning [*Thybo et al*., 2000]. There is no clear surface expression of a transfer fault zone between the northern and southern ends of the Songo and Nguruman border faults, respectively, which exhibit a small, soft-linked, right step-over (~10 km offset) (Figures 1, 6, and 7).

Natron basin: Excluding the volcanic zone at the southern end of the basin, nodal planes of focal mechanisms indicate slip along steep planes (Tables 1 and 2 and Figure 7). Seismicity in the Natron basin north of Oldoinyo Lengai volcano is localized to the western side of the basin, and to the zone of closely spaced NNE-striking faults and aligned eruptive centers cutting the Gelai shield complex. The western zone of seismicity includes lower crustal earthquakes that lie along a subsurface projection of the Songo border fault, which dips ~60° at the surface [*Foster et al*., 1997; *Le Gall et al*., 2008] (Figure 9a). Hot springs and soil gas measurements record large CO_2 emissions along the length of the Songo border fault system, as well as the fault system on the western side of Gelai volcano [*Lee et al*., 2016]. A second N-S trending zone of lower crustal seismicity occurs about 15 km to the east of the border fault, near the center of the basin, and it rises to ~6 km below sea level (Figure 9a). Excluding event 49, focal mechanisms beneath the eastern side of Lake Natron show slip along steep, N-S to NNE-striking fault planes (Figure 7).

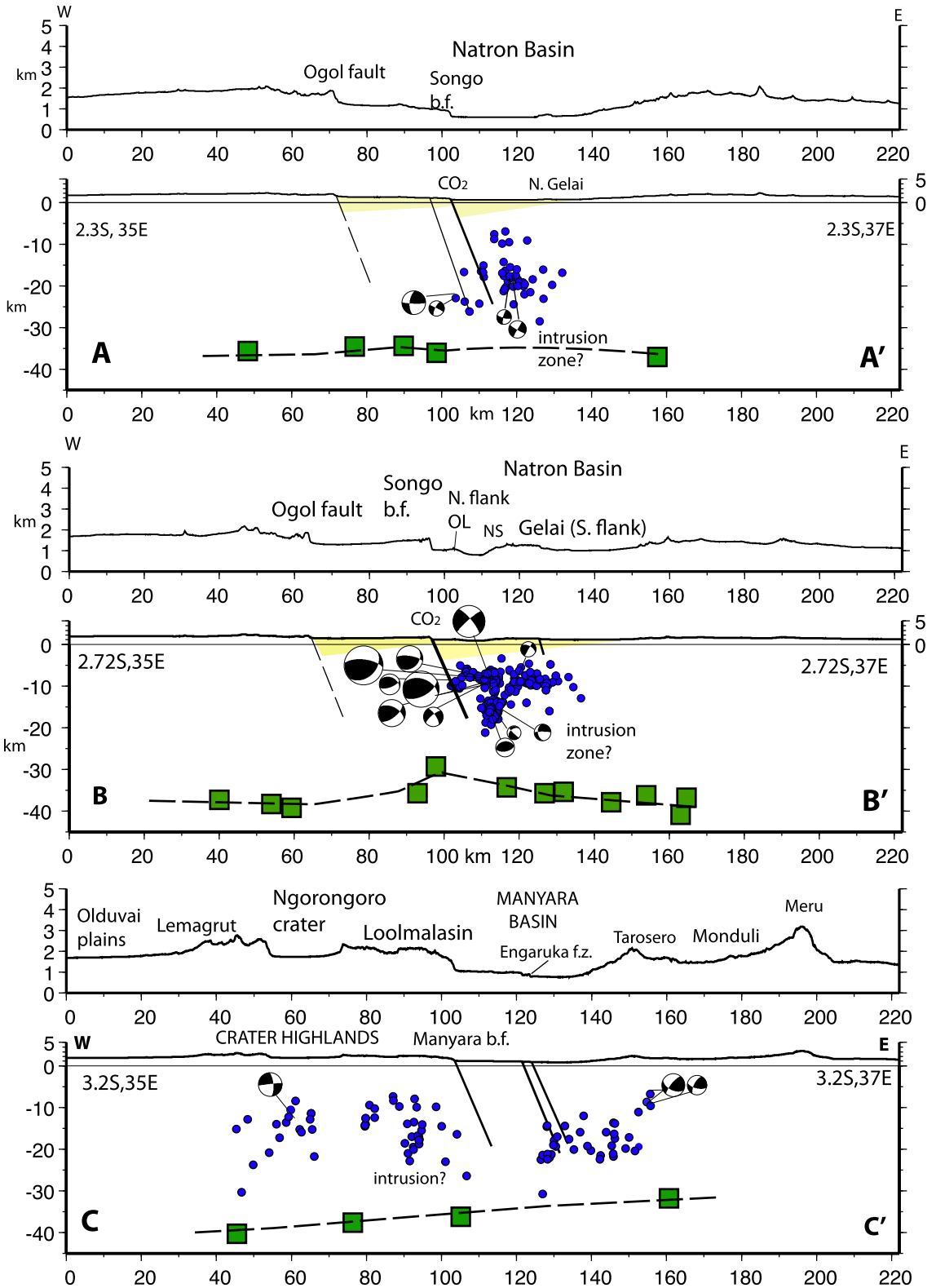

Figure 9. True-scale cross sections with vertically exaggerated topography (VE 5:1) above, as located on Figures 6 and 7. Cross sections compare double-difference relocations (blue) and focal mechanisms projected into the line of the profiles from 5 km N and S of the profile. Green squares are centered on Moho depth estimates from receiver functions projected from 10 km N and S of profiles, with size approximately the same as depth errors, from *Plasman et al*. [2017]. "CO_2" indicates site of significant fault zone degassing [*Lee et al*., 2016]. Profile A–A′ crosses the central Natron basin; Profile B–B′ crosses the southern Natron basin and the Naibor Soito monogenetic volcanic field, and Profile C–C′ crosses the Crater Highlands, northern Manyara border fault, and Engaruka transfer fault zone (Figure 1). Figure 10b is an enlargement of Profile B between 77 and 143 km.

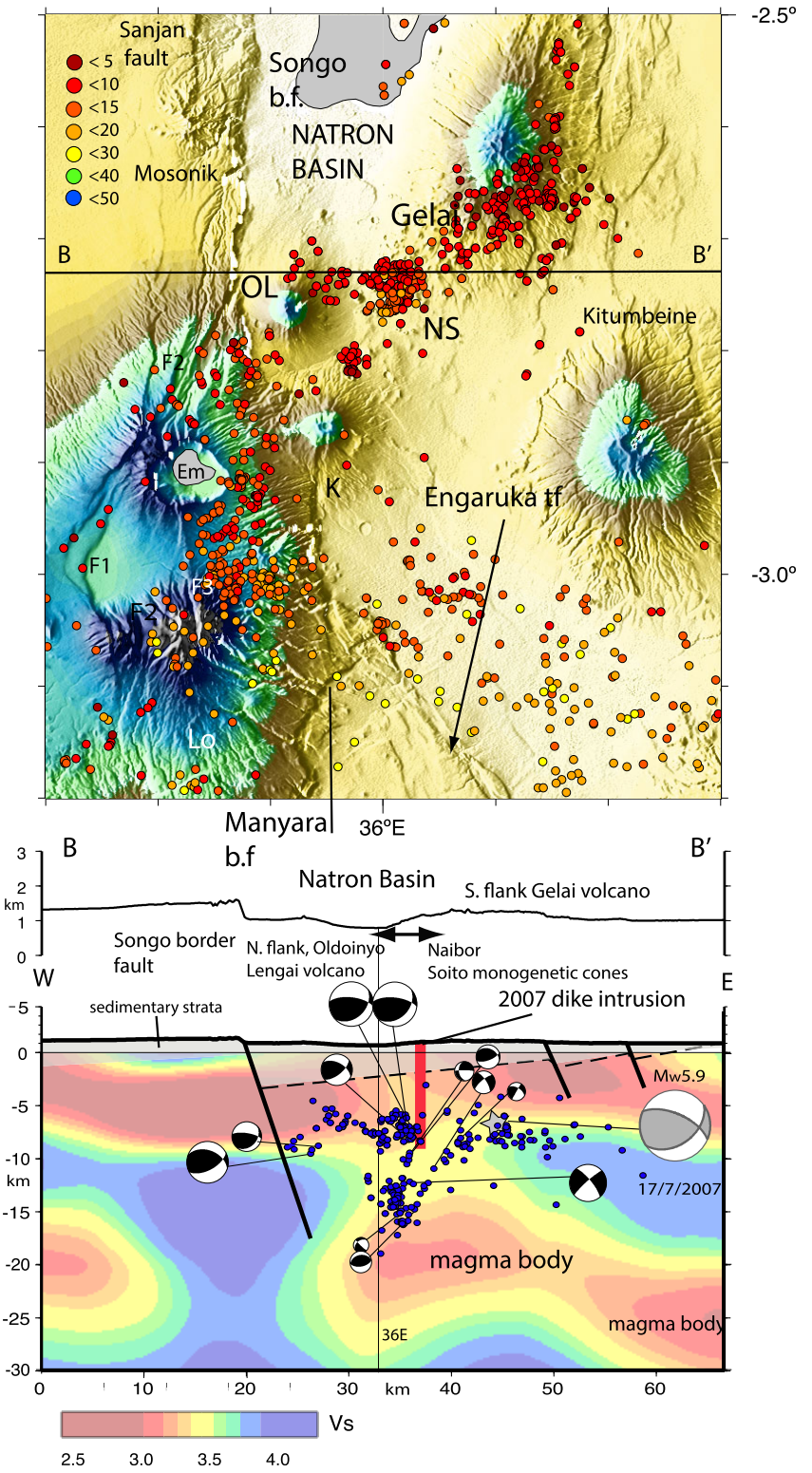

Figure 10. Enlargement of double-difference clustered earthquake locations (Figure 6) and rift cross section shown in Figure 9b overlying detail of 3-D velocity model from joint arrival-time, ambient noise, and gravity inversion [*Roecker et al.*, 2017]. Topography above the cross section has a VE of 2; detailed structural interpretation in *Muirhead et al.* [2016]. The bold red line is the geometry of the July 2007 dike intrusion from inversion of InSAR data [*Wauthier*, 2011]. Gray focal mechanism for the Mw 5.9 17 July 2007 earthquake is determined using global and local seismic data [*Calais et al.*, 2008]. Note that CRAFTI-CoLiBrEA earthquakes from both shallow and deep zones show similar mechanisms. F1, F2 are unnamed faults.

Moho depths across the Natron basin vary from about 40 km beneath the flanks of the rift, to 27 km beneath Lake Natron, suggesting as much as 30% extension across this basin (Figures 9a and 9b). Low S-velocity zones as well as high Vp/Vs ratios in the lower crust beneath Lake Natron suggest widespread magmatic underplate [*Plasman et al*., 2017; *Roecker et al*., 2017], providing a source for the high levels of CO_2 degassing along the Songo border fault. Receiver functions show a strong impedance contrast at the crust-mantle interface, a pattern consistent with the high reflectivity lower crust interpreted as underplate beneath the Magadi and Natron basins [*Thybo et al*., 2000; *Plasman et al*., 2017]. Considering the lower crustal seismicity we detect, and these independent constraints, the western Natron basin may be the site of active underplating and intrusion.

Oldoinyo Lengai-Naibor Soito-Gelai (OL-NS-G) volcanic chain: The majority of earthquakes we located form a NE-trending belt between Embagai volcano on the Crater Highlands and Gelai volcano in the central Natron basin (Figures 1, 4, and 6). Excluding the Naibor Soito cone complex, seismicity spans the base of crust to surface, and it encompasses the site of the 2007–2008 seismovolcanic crisis. Notable is the N-S trending belt of frequent, shallow seismicity between Loolmalasin volcano and Embagai volcano that rotates NE between Oldoinyo Lengai and Gelai volcanoes (Figures (1 and 4), and 6). Focal mechanisms between Loolmalasin and the Naibor Soito cone complex show two subsets: approximately N-S planes, and N50–80°E planes that match the distribution pattern (Figure 7). The cluster of shallow earthquakes beneath the southern and eastern flanks of Gelai volcano have a wide range of nodal planes ranging from ~E-W to NW, whereas normal faults and aligned cones strike ~E-W and NNE [*Muirhead et al*., 2015].

Geodetic and seismic data show that 50–65% of the strain release during the 2007–2008 seismovolcanic crisis in the Natron basin was accommodated aseismically, consistent with the intrusion of a 7–15 km-long, ~2.4 m-wide, ~4 km-high dike beneath the Naibor Soito complex [*Calais et al*., 2008] (Figure 1). Considering the relocations of some earthquakes using a local array and surface fractures [*Albaric et al*., 2014; *Wauthier*, 2011], the 2007 teleseisms in Figure 3 should be shifted to the southern Gelai region. The 2007 hypocentral depths are 5–10 km, somewhat shallower than the 6–16 km depths for local earthquakes that we determine from precise relocations.

In cross section (Figure 10), seismicity clusters around the boundaries of low-velocity zones within the lower crust imaged in crustal tomography and interpreted as degassing magma bodies, and at the edges of strong velocity contrasts where stress concentrations are expected [*Roecker et al*., 2017]. Planform and cross sections of seismicity suggest that the Naibor Soito cone field is underlain by two disk-shaped zones with eastern edge at 36°E, and at depth between 6.5–8 km below sea level (Figures 9b and 10). These stacked zones of seismicity beneath the <1 Ma Naibor Soito monogenetic cone complex may be pressurized sills sourced by hot, gas-rich magmatic fluids from the lower crustal magma chamber (Figure 10). Their spatial location is consistent with one model for the source of magmas for the 2007 dike intrusion: ~10 km depth beneath the Naibor Soito complex [*Calais et al*., 2008]. Crustal tomography shows elevated *P* and *S* wave velocities in the upper crust beneath Naibor Soito where mafic lavas have been erupted (Figure 10). The higher velocities may be caused by repeated intrusions of olivine-rich melilitite with abundant mantle fragments that would also increase density and velocity [*Mattsson et al*., 2013; *Manya*, 2014]. A second subset of well-clustered earthquakes at <10 km depth rises NW to the flank of Oldoinyo Lengai volcano. The shape of this smaller cluster is also circular in planform (Figure 10).

The two M_L 4.7 normal fault earthquakes in the 3–4 June 2013 swarm initiated at the edge of a disk-shaped zone of seismicity interpreted as a sill complex, a time-space pattern nearly identical to the start of the 2007 volcanotectonic crisis in the same area [*Baer et al*., 2008; *Calais et al*., 2008]. The 2007 dike intrusion zone determined from models of InSAR data coincides with the eastern edge of the tabular zones, and the June 2013 focal mechanisms are similar to those of the 17 July 2007 Mw 5.9 earthquake that preceded and potentially triggered the 2007 dike intrusion (Figures 9b and 10). Based on these similarities and new imaging, the July 2007 dike intrusion was most likely sourced from the Naibor Soito sill complex. A similar stacked sill complex is interpreted from combined seismicity and petrological studies of composite and shield volcanoes in Afar [e.g., *Field et al*., 2012].

Crater Highlands and Engaruka Transfer Fault Zone: The N-S-striking Songo border fault is linked to the NNE-trending Manyara border fault via the NW-striking oblique-slip Engaruka fault system, which bounds a narrow depression (Figure 1). Event 63 (~10 km depth) occurred near the Manyara-Engaruka fault intersection,

and its N-S subvertical nodal plane suggests slip along the Manyara border fault (Figure 7). Event 65 (~9 km depth) shows slip along a NW-striking nodal plane parallel to the Engaruka fault. Events 39 and 64 beneath the Lembolos graben (Figure 1) have steep NW-striking nodal planes that parallel local vent alignments [*Muirhead et al*., 2015], suggesting that this WNW-striking faulted depression continues beneath the volcanic chain (e.g., Figure 9c). The NW-striking surface faults, persistent and widely distributed seismicity, and eruptive volcanic chains suggest that the Engaruka fault transfers strain from the Natron-Manyara rift sector eastward to the Pangani rift, consistent with time-averaged deformation patterns [*Le Gall et al*., 2008; *Muirhead et al*., 2015] (Figures 1 and 4).

Clustered earthquake swarms occur along N-S and NE-striking fault planes within the Crater Highlands (Figures 7 and 9c). Notable are the pipe-like swarm of earthquakes beneath Loolmalasin volcano, and the diffuse midcrustal swarm beneath Ngorongoro crater (Figures 1 and 9c). Events 35 and 36 are midcrustal earthquakes with steep slip planes that may have occurred along projections of NNE-striking normal faults on the western side of Ngorongoro and Olmoti volcanoes (Figures 1 and 7). N-S-striking faults F2 west of Embagai, F3 cutting Olmoti caldera and Oldeani volcano are also active (Figure 2).

Manyara basin: Most of the earthquake activity occurs south of 3.6°S, and outside our array, with spatial distribution similar to that documented by *Albaric et al*. [2014] and *Mulibo and Nyblade* [2009].

6.2. Stress Field Rotation at OL-NS-G Volcanic Chain

Seismic and geodetic data from the Eastern rift indicate approximately E-W extension along the Eastern rift, with the OL-NS-G volcanic chain a local exception: NNW-SSE directed extension. The localized nature of the extension direction argues against the involvement of basement fabric, as outlined below. *Le Gall et al*. [2008] interpreted the shift from N-S striking fault to NE-striking faults and dikes within the southern Natron basin as evidence for basement control on fault orientations. *Muirhead et al*. [2015] synthesized dike data from the study area, and found subradial patterns around the largest constructs, and only local agreement with the NE-striking strain fabric and dike swarms in Archaean rocks [e.g., *Mudd and Orridge*, 1966; *Halls et al*., 1987; *Le Gall et al*., 2008]. The Archaean and Pan-African strain fabrics, moreover, dip at angles $\leq 45°$ [e.g., *Smith and Mosley*, 1993] that are much shallower than the subvertical dip angle of the 2007 dike, and earlier dikes [*Calais et al*., 2008; *Biggs et al*., 2009, 2013; *Muirhead et al*., 2015]. Preferential reactivation of generally shallow-dipping basement fabrics, therefore, seems unlikely as the cause of the local stress field rotation, which is not seen north and south of the OL-NS-G chain where basement fabric is also NE.

Based on the along-axis patterns of faulting and magmatism, we interpret a local rotation in extension direction in the area of widespread, and currently active magma intrusion from Embagai to Gelai volcano. The NNE-elongate surface and internal loads add to the ~E-W extensional tectonic stress field, and cause a local and possibly temporal rotation in the stress field [e.g., *de Vries and Merle*, 1996; *Gudmundsson*, 2006; *Karlstrom et al*., 2009] (Figures 8 and 11). Numerical and analytical modeling in progress tests the role of rift morphology and surface and subsurface loading on the observed changes in dike and fault kinematics [e.g., *Maccaferri et al*., 2014].

Geological data suggest that the local extension direction rotation existed before the 2007 dike intrusion-eruption sequence, and perhaps before 0.35 Ma. Not only do dikes and aligned volcanic chains strike NE, but the inferred swarm of dikes in the Gelai region [*Muirhead et al*., 2015] appear to merge with ~1 Ma Kerimasi volcano, which lies immediately to the south of Oldoinyo Lengai (Figure 1). Kerimasi and Gelai volcanoes formed contemporaneously [*Mana et al*., 2015], and a NE-trending magma intrusion zone may have served to transfer magma and strain from the Manyara border fault to Gelai volcano at 1 Ma, before Oldoinyo Lengai developed at about 0.35 Ma [e.g., *Sherrod et al*., 2013].

The sustained activity between the northern tip of the Manyara border fault and Gelai volcano suggests that the geometry and kinematics of intrabasin linkage zones in magmatic rifts are strongly influenced by the spatial arrangement of crustal magma chambers during the early stages of rifting. In the Eastern rift case, the stress field rotation facilitates strain transfer from the Manyara border fault system, the locus of deformation during the earliest stages of rifting, to the zone of magma intrusion in the central rift valley. The Natron border fault is seismically active as well as the subvertical zones of lower crust to surface seismicity in the central basin, interpreted as the site of repeated dike intrusions. Structural analyses [*Muirhead et al*., 2016] and our studies indicate that older, 7 Ma Nguruman border fault is largely inactive, and strain

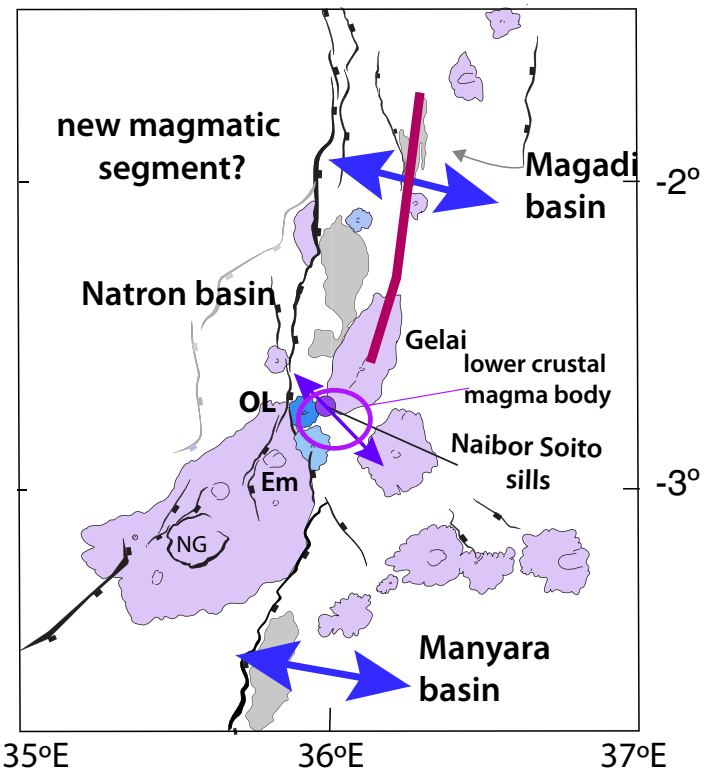

Figure 11. Simple schematic model illustrating local extension direction rotation along the length of the Eastern rift and geometry of strain transfer from the Manyara border fault to the central rift valley zone of magmatism and intrabasinal faulting. From Oldoinyo Lengai (OL) volcano northward, the locus of strain appears to migrate to the central rift valley in a pattern similar to magmatic segments in the Main Ethiopian rift and Afar Depression. Magma intrusions from the NE-trending line of active eruptive centers above a lower crustal magma chamber (purple ellipse) and stacked sills (filled purple circle) between Embagai crater (Em) and Gelai volcano facilitate strain transfer to the central basin, and the surface and subsurface loads are associated with a local rotation in opening direction. Lakes are shaded gray, basaltic and composite volcanoes violet, and carbonatite volcanoes are indicated in blue shades.

has migrated to a ~30 km-wide zone of dike intrusion and faulting in the Lake Magadi area. The spatial patterns of faulting and magmatism from Gelai northward in the Eastern rift system is very similar to that of the Main Ethiopian and Afar rift systems where strain is localized to ~20 km-wide, ~50 km-long magmatic segments that are sites of regular magma intrusion fed from one or more crustal magma chambers [e.g., *Keranen et al*., 2004; *Bendick et al*., 2006; *Keir et al*., 2009] (Figure 11).

6.3. Lower Crustal Earthquakes

Do fluids released from magma degassing and mantle metasomatism cause overpressure that adds to normal stress, and induces seismicity [e.g., *Keir et al*., 2009; *Lindenfeld et al*., 2012]? Does the presence of fluids near border faults cause fault zone weakening and microseismicity [*Reyners et al*., 2007]? Or, is the lower crust unusually strong beneath East Africa [*Shudofsky*, 1985; *Mulibo and Nyblade*, 2009; *Yang and Chen*, 2010; *Craig et al*., 2011]?

Crustal xenoliths from Archaean crust and Pan-African crust (Lashaine, Naibor Soito) are mafic granulites [*Jones et al*., 1983; *Mansur et al*., 2014], indicating similar lower crustal compositions on either side of the Archaean-Pan-African suture (Figure 2). *Sippel et al*. [2017] reexamine controlled source, mantle tomography, and heat flow data from the Eastern rift in Kenya and Tanzania, and also infer granulite lower crust. Laboratory experiments simulating lower crustal conditions demonstrate that granulite in the lower crust is relatively weak, particularly if the rock contains a small weight percent of water [*Wang et al*., 2012]. Using these stress-strain relations for mafic granulite and strain rates and geotherms from *Sippel et al*. [2017], the brittle-ductile transition occurs between 15 and 16 km below sea level (assuming 12 MPa/km gradient as in *Behr and Platt* [2011] and supporting information Figure SM11), or much lower than estimates used in *Sippel et al*. [2017]. The widespread metasomatism, degassing at the surface, and hydration of mantle xenoliths all suggest that the calculated yield stress for mafic granulite is an upper bound on strength of the crust beneath the Magadi-Natron-Manyara area, providing little explanation for the $M_L > 2.5$ earthquakes beneath the Magadi-Natron basins from our work, and earlier studies by *Ibs-von Seht et al*. [2001]. The Manyara basin has even deeper earthquakes, with teleseisms at 30–35 km [*Yang and Chen*, 2010], and the majority of local earthquakes between 30 and 40 km [*Albaric et al*., 2014].

Cooled magmatic underplate beneath parts of the Magadi and Natron basins may locally strengthen the lower crust, but high Vp/Vs ratios in the lower crust and CO_2 degassing along faults that penetrate to the lower crust indicate fluid alteration, compressible fluids in pore spaces, and local heating, consistent with active underplating that weakens the crust [*Plasman et al*., 2017; *Roecker et al*., 2017]. A strong, mafic lower

crust, therefore, seems an unlikely explanation for widespread lower crustal seismicity in the magmatically active Natron and Magadi basins.

One subset of lower crustal earthquakes occurs along lower crustal projections of Natron basin (Songo) border faults that are actively degassing magmatic CO_2 [*Lee et al*., 2016, 2017], and where Vp/Vs is unusually low [*Roecker et al*., 2017]. The border faults, therefore, provide fluid pathways to the surface for exsolved gases from the active zones of underplating in the lower crust. The CO_2 gas exsolved from active magma intrusion is a dense, super critical fluid in the lower crust, and its presence may preferentially embrittle the stretched and intruded granulitic lower crust [e.g., *Selverstone and Wawrzyniec*, 2001]. Exsolving volatiles may create a lower threshold for rock failure by increasing pore pressures in country rock surrounding or above degassing magma bodies [e.g., *Sibson*, 1992; *Collettini et al*., 2008]. Although little is known of CO_2 in the lower crust, its presence promotes cataclasis, pressure solution, and phyllosilicate formation, all of which reduce friction and promote fault creep [*Niemeijer and Spiers*, 2005; *Collettini et al*., 2008]. The CO_2 release, therefore, may serve to localize strain to the border fault during early-stage rifting, and explain some of the seismicity at depth greater than the brittle-ductile transition for mafic granulite in this area ($\sim$15 km below sea level).

A second subset of lower crustal earthquakes appears to be directly associated with magma and volatile migration. The lower crustal low-velocity zone beneath the Naibor Soito monogenetic cone complex is largely aseismic, and it is surrounded by a zone of persistent seismicity. This lower crustal low-velocity zone likely indicates a pressurized magma body. Resolution tests of crustal tomography models argue against the presence of two separate magma chambers beneath Oldoinyo Lengai and Naibor Soito cone province, indicating that the Oldoinyo Lengai eruptions, and intrusions into the upper crust beneath the Naibor Soito monogenetic cone province may be sourced from the same magma chamber [*Roecker et al*., 2017]. The Naibor Soito sill and dike complex, therefore, may provide hydraulic connection to Oldoinyo Lengai volcano, and feed dike intrusions into the monogenetic cone province. Stressing of lower crust by both gas and magma movement, volatile migration, and fluid overpressure, therefore, are the likely causes of lower crustal earthquakes in the magma-rich Natron and Magadi basins.

6.4. Implications for Earthquake and Volcanic Hazards

We detect two or more pressurized magma chambers and intrusive bodies beneath the Natron-Manyara accommodation zone: the lower crustal magma chamber beneath Oldoinyo Lengai, Naibor Soito monogenetic cone complex, and southern Gelai volcano, and a sill complex at 6–10 km between Oldoinyo Lengai and Gelai volcanoes. Earthquake hazard models are commonly linked to repeat times of large earthquakes that relieve tectonic stress, but the large difference in geodetic and seismic energy release suggests that some tectonic stress may persist. The decadal eruption cycle at Oldoinyo Lengai volcano indicates that the volcano recharge cycle is much shorter than tectonic cycles, and lead to more complex time-space seismicity patterns. Our active deformation studies indicate that earthquakes are largely driven by stress state around inflating magma bodies, and more dike intrusions with surface faulting, eruptions with sometimes large volume ash and lapilli ejecta, and frequent M4–6 earthquakes are expected. The curvature in the cumulative frequency versus magnitude relation for the OL-NS-G window is caused by an apparently larger number of $2.7 < M_L < 5$ earthquakes around the sill complexes, where rupture length may be constrained [e.g., *Main*, 1987].

Eruptions in the monogenetic cone complex are also a hazard. Petrological analyses of lavas erupted in the monogenetic cone province above the Naibor Soito magma body indicate very rapid ($<$48 h) mantle-to-surface ascent of CO_2-rich olivine melilitites [*Mattsson and Tripoli*, 2011], indicating that future eruptions could occur with little or no warning, and be accompanied by damaging earthquakes. The sill complex between Oldoinyo Lengai and Gelai volcanoes leaves open the possibility of magma mixing and stress triggering between volcanoes, and may explain the 2007 earthquake-dike-eruption sequence. Shaking from persistent and very shallow $\leq$6 km earthquakes beneath the Crater Highlands could trigger landslides down the steep fault scarps. Planned and future development in the national parks and game reserves should proceed with awareness of these active ground deformation and potential eruption and gas release hazards, and include long-term geophysical and geochemical monitoring.

7. Conclusions

The CRAFTI-CoLiBrEA broadband seismic array was used to locate 3427 earthquakes over a 13 month period between January–February 2013 and 1 December 2013 to 6 December 2014, including earthquakes within the deeply rooted Archaean craton. Earthquakes within the array were relocated using waveform cross correlation of events in a double-difference earthquake relocation algorithm, taking advantage of a new 3-D velocity model derived from our data. We determine a new earthquake magnitude scaling relation that accounts for local attenuation effects, and find agreement between local magnitudes and body wave magnitudes for two teleseisms that occurred during our experiment. The *b*-value for the entire data set ($N = 2315$) is 0.87 ± 0.03, similar to earlier estimates for the craton and rift zone.

Some of the precisely relocated events occur at depths of 20–27 km along subsurface projections of border faults, constraining fault dips to 50° or more in the lower crust. The fault zones serve as conduits to the surface for CO_2 exsolved from active magma intrusion into the lower crust beneath much of the study area. The magmatic CO_2 release, therefore, explains some of the seismicity at depth greater than the brittle-ductile transition for mafic granulite in this area (∼15 km below sea level). Rock-CO_2 interactions promote creep, serving to localize strain to the border fault during early-stage rifting. Lower crustal seismicity occurs around pressurized magma chambers where high fluid pressures induce hydraulic fracture. Intense, tabular shaped clusters of earthquakes between 6 and 10 km depth, including two M_L 4.7 earthquakes beneath the Naibor Soito monogenetic cone province, are interpreted as a stacked sill complex above a lower crustal low-velocity zone interpreted by *Roecker et al*. [2017] as a magma chamber.

Focal mechanism analyses of local earthquakes and consideration of mechanisms of previous instrumentally recorded earthquakes indicate a local rotation in extension direction from ∼E-W to SSE in the area of active magma intrusion between Oldoinyo Lengai, Naibor Soito monogenetic cone complex, and Gelai volcano. The stress field rotation facilitates strain transfer from the border fault system, the locus of deformation during the earliest stages of rifting, to the zone of magma intrusion in the central rift valley. The ∼60° rotation in T axis direction across the magmatically active Natron-Manyara accommodation zone relative to rift sectors to the north and south may be caused by low density lower crustal magma body and surface topography that superposes a radial stress field on the tectonic extension direction. Our active deformation studies indicate that earthquakes are largely driven by stress state around inflating magma bodies, and more dike intrusions with surface faulting, eruptions, and frequent M4–6 earthquakes are expected.

Acknowledgments

This research was supported by NSF grant EAR-1113355 (C.E., S.R., J.M., T.F., A.W., M.A., C.L., A.R., and E.W.), grant ANR-12-JS06–000401 (C.T., J.A., S.G., and S.P.), and with approval by the Commission for Science and Technology (Tanzania) and the National Council for Science and Technology (Kenya). The seismic instruments were provided by the Incorporated Research Institutions for Seismology (IRIS) through the PASSCAL Instrument Center at New Mexico Tech. Data collected will be available through the IRIS Data Management Center. The facilities of the IRIS Consortium are supported by the National Science Foundation under Cooperative Agreement EAR-1261681 and the DOE National Nuclear Security Administration. We are grateful for logistical support from Tanzania National Parks Commission and to the Ngorongoro National Park. We could not have achieved this work without logistical assistance from primary and secondary school teachers throughout the region, the Maasai clans in Kenya and Tanzania, and driver-guides from Fortes Tours. A. Palardy assisted with fieldwork; C. Drooff, D. Trail, and C. Marone provided insights into lower crustal gas-rock interactions. We thank Editor T. Becker, E. Rivalta, and two anonymous reviewers for constructive comments that improved this manuscript. Graphs were made using Generic Mapping Tools (www.soest.hawaii.edu/gmt) [*Wessel and Smith*, 1998].

References

Aki, K. (1965), Maximum likelihood estimate of b in the formula logN = a – bM and its confidence limits, *Bull. Earthquake Res. Inst., Tokyo Univ*., 43, 237–239.

Albaric, J., J. Perrot, J. Déverchère, A. Deschamps, B. Le Gall, R. Ferdinand-Wambura, C. Petit, C. Tiberi, C. Sue, and M. Songo (2010), Contrasted seismogenic and rheological behaviours from shallow and deep earthquake sequences in the North Tanzanian Divergence, East Africa, *J. Afr. Earth Sci.*, *58*(5), 799–811, doi:10.1016/j.jafrearsci.2009.09.005.

Albaric, J., J. Déverchère, J. Perrot, A. Jakovlev, and A. Deschamps (2014), Deep crustal earthquakes in North Tanzania, East Africa: Interplay between tectonic and magmatic processes in an incipient rift, *Geochem. Geophys. Geosyst.*, *15*, 374–394, doi:10.1002/2013GC005027.

Amelung, F., and G. King (1997), Large-scale tectonic deformation inferred from small earthquakes, *Nature*, *386*(6626), 702–705.

Aulbach, S., R. L. Rudnick, and W. F. McDonough (2008), Li-Sr-Nd isotope signatures of the plume and cratonic lithospheric mantle beneath the margin of the rifted Tanzanian craton (Labait), *Contrib. Mineral. Petrol.*, *155*(1), 79–92.

Aulbach, S., R. L. Rudnick, and W. F. McDonough (2011), Evolution of the lithospheric mantle beneath the East African Rift in Tanzania and its potential signatures in rift magmas, *Spec. Pap. Geol. Soc. Am.*,478, 105–125.

Baer, G., Y. Hamiel, G. Shamir, and R. Nof (2008), Evolution of a magma-driven earthquake swarm and triggering of the nearby Oldoinyo Lengai eruption, as resolved by InSAR, ground observations and elastic modeling, East African Rift, 2007, *Earth Planet. Sci. Lett.*, *272*(1), 339–352.

Baker, B. H. (1986), Tectonics and volcanism of the southern Kenya Rift Valley and its influence on rift sedimentation, *Geol. Soc. Spec. Publ.*, *25*(1), 45–57.

Behr, W. M., and J. P. Platt (2011), A naturally constrained stress profile through the middle crust in an extensional terrane, *Earth Planet. Sci. Lett.*, *303*, 181–192.

Belachew, M., C. Ebinger, D. Coté, D. Keir, J. V. Rowland, J. O. S. Hammond, and A. Ayele (2011), Comparison of dike intrusions in an incipient seafloor-spreading segment in Afar, Ethiopia: Seismicity perspectives, *J. Geophys. Res.*, *116*, B06405, doi:10.1029/2010JB007908.

Bendick, R., S. McClusky, R. Bilham, L. Asfaw, and S. Klemperer (2006), Distributed Nubia—Somalia relative motion and dike intrusion in the Main Ethiopian Rift, *Geophys. J. Int.*, *165*(1), 303–310.

Biggs, J., F. Amelung, N. Gourmelen, T. H. Dixon, and S. Kim (2009), InSAR observations of 2007 Tanzania rifting episode reveal mixed fault and dyke extension in an immature continental rift, *Geophys. J. Int.*, *179*, 549–558.

Biggs, J., M. Chivers, and M. Hutchison (2013), Surface deformation and stress interactions during the 2007–2010 sequence of earthquake, dyke intrusion, and eruption in northern Tanzania, *Geophys. J. Int.*, *195*, 16–26.

Birhanu, Y., R. Bendick, S. Fisseha, E. Lewi, M. Floyd, R. King, and R. Reilinger (2016), GPS constraints on broad scale extension in the Ethiopian Highlands and Main Ethiopian Rift, *Geophys. Res. Lett.*,*43*, 6844–6851, doi:10.1002/2016GL069890.

Birt, C. S., P. K. H. Maguire, M. A. Khan, H. Thybo, G. R. Keller, and J. Patel (1997), The influence of pre-existing structures on the evolution of the southern Kenya Rift Valley—Evidence from seismic and gravity studies, *Tectonophysics*, *278*(1), 211–242, doi:10.1016/S0040-1951(97)00105-4.

Bott, M. H. P. (1959), The mechanics of oblique slip faulting, *Geol. Mag.*, *96*(2), 109–117.

Brazier, R. A., A. A. Nyblade, and J. Florentin (2005), Focal mechanisms and the stress regime in NE and SW Tanzania, East Africa, *Geophys. Res. Lett.*, *32*, L14315, doi:10.1029/2005GL023156.

Buck, W. R. (2004), Consequences of asthenospheric variability on continental rifting, in *Rheology and Deformation of the Lithosphere at Continental Margins*, edited by G. D. Karner et al., pp. 1–31, Columbia Univ. Press, New York.

Calais, E., et al. (2008), Strain accommodation by slow slip and dyking in a youthful continental rift, East Africa, *Nature*, *456*(7223), 783–787.

Chesley, J. T., R. L. Rudnick, and C. T. Lee (1999), Re-Os systematics of mantle xenoliths from the East African Rift: Age, structure, and history of the Tanzanian craton, *Geochim. Cosmochim. Acta*, *63*(7), 1203–1217.

Collettini, C., C. Cardellini, G. Chiodini, N. De Paola, R. E. Holdsworth, and S. A. F. Smith (2008), Fault weakening due to CO_2 degassing in the Northern Appennines: Short- and long-term processes, in *The Internal Structure of Fault Zones: Implications for Mechanical and Fluid-Flow Properties*, edited by C. A. J. Wibberley et al., Geol. Soc. Spec. Publ., 299, 175–194.

Craig, T. J., J. A. Jackson, K. Priestley, and D. P. McKenzie (2011), Earthquake distribution patterns in Africa: Their relationship to variations in lithospheric and geological structure, and their rheological implications, *Geophys. J. Int.*, *185*(1), 403–434.

Dawson, J. B. (1992), Neogene tectonics and volcanicity in the North Tanzania sector of the Gregory Rift Valley: Contrasts with the Kenya sector, *Tectonophysics*, *204*, 81–92.

de Vries, B. V. W., and O. Merle (1996), The effect of volcanic constructs on rift fault patterns, *Geology*, *24*, 643–646.

Delcamp, A., D. Delvaux, S. Kwelwa, A. Macheyeki, and M. Kervyn (2016), Sector collapse events at volcanoes in the North Tanzanian divergence zone and their implications for regional tectonics, *Geol. Soc. Am. Bull.*, *128*(1–2), 169–186.

Desissa, M., N. E. Johnson, K. A. Whaler, S. Hautot, S. Fisseha, and G. J. K. Dawes (2013), A mantle magma reservoir beneath an incipient mid-ocean ridge in Afar, Ethiopia, *Nat. Geosci.*, *6*(10), 861.

Dziewonski, A. M., T.-A. Chou, and J. H. Woodhouse (1981), Determination of earthquake source parameters from waveform data for studies of global and regional seismicity, *J. Geophys. Res.*, *86*, 2825–2852.

Ebinger, C., and C. A. Scholz (2012), Continental rift basins: An East African perspective, in *Sedimentary Basins*, edited by C. Busby and A. Azor, pp. 183–208, John Wiley and Sons Ltd., Chichester, UK, doi:10.1002/9781444347166.ch9.

Ebinger, C. J., J. van Wijk, and D. Keir (2013), The time scales of continental rifting: Implications for global processes, in *Tectonics: 50 Years After The Revolution, The Web of Geological Sciences: Advances, Impacts, and Interactions*, edited by M. Bickford, *Spec. Pap. Geol. Soc. Am.*, 500, 371–396.

Engdahl, E. R., R. van der Hilst, and R. Buland (1998), Global teleseismic earthquake relocation with improved travel times and procedures for depth determination, *Bull. Seismol. Soc. Am.*, *88*(3), 722–743.

Field, L., J. Blundy, R. A. Brooker, T. Wright, and G. Yirgu (2012), Magma storage conditions beneath Dabbahu Volcano (Ethiopia) constrained by petrology, seismicity and satellite geodesy, *Bull. Volcanol.*, *74*(5), 981–1004.

Fischer, T. P., P. Burnard, B. Marty, D. R. Hilton, E. Füri, F. Palhol, and F. Mangasini (2009), Upper-mantle volatile chemistry at Oldoinyo Lengai volcano and the origin of carbonatites, *Nature*, *459*(7243), 77–80.

Foster, A., C. J. Ebinger, E. Mbede, and D. Rex (1997), Tectonic development of the northern Tanzanian sector of the East African Rift System, *J. Geol. Soc.*, *154*(4), 689–700.

Foster, A. N., and J. A. Jackson (1998), Source parameters of large African earthquakes: Implications for crustal rheology and regional kinematics, *Geophys. J. Int.*, *134*, 422–448.

GEOFON Data Centre (1993), *GEOFON Seismic Network*, Dtsch. Geo Forsch. Zent., Other/Seismic Network, Potsdam, Germany, doi:10.14470/TR560404.

Grandin, R., et al. (2009), September 2005 Manda Hararo-Dabbahu rifting event, Afar (Ethiopia): Constraints provided by geodetic data, *J. Geophys. Res.*, *114*, B08404, doi:10.1029/2008JB005843.

Green, W. V., U. Achauer, and R. P. Meyer (1991), A three-dimensional seismic image of the crust and upper mantle beneath the Kenya rift, *Nature*, *354*(6350), 199–207.

Gudmundsson, A. (2006), How local stresses control magma-chamber ruptures, dyke injections, and eruptions in composite volcanoes, *Earth Sci. Rev.*, *79*(1), 1–31.

Guerri, M., F. Cammarano, and J. A. Connolly (2015), Effects of chemical composition, water and temperature on physical properties of continental crust, *Geochem. Geophys. Geosyst.*, *16*, 2431–2449, doi:10.1002/2015GC005819.

Gutenberg, B., and C. F. Richter (1944), Frequency of earthquakes in California, *Bull. Seismol. Soc. Am.*, *34*(4), 185–188.

Halls, H. C., K. G. Burns, S. J. Bullock, and P. M. Batterham (1987), Mafic dyke swarms of Tanzania interpreted from aeromagnetic data, in *Mafic Dyke Swarms*, edited by H. Halls and W. Fahrig, *Spec. Pap. Geol. Soc. Can.*, 34, 173–186.

Hollnack, D., and R. Stangl (1998), The seismicity related to the southern part of the Kenya Rift, *J. Afr. Earth Sci.*, *26*(3), 477–495.

Ibs-von Seht, M., S. Blumenstein, R. Wagner, D. Hollnack, and J. Wohlenberg (2001), Seismicity, seismotectonics and crustal structure of the southern Kenya Rift—New data from the Lake Magadi area, *Geophys. J. Int.*, *146*(2), 439–453.

Illsley-Kemp, F., D. Keir, J. M. Bull, A. Ayele, J. O. Hammond, J. M. Kendall, R. J. Gallacher, T. Gernon, and B. Goitom (2017), Local earthquake magnitude scale and b-value for the Danakil region of northern Afar, *Bull. Seismol. Soc. Am.*, *107*(2), 521–531.

Jackson, J., and D. McKenzie (1988), The relationship between plate motions and seismic moment tensors, and the rates of active deformation in the Mediterranean and Middle East, *Geophys. J. Int.*, *93*(1), 45–73.

Jones, A. P., J. V. Smith, B. Dawson, and E. C. Hansen (1983), Metamorphism, partial melting, and K-metasomatism of garnet-scapolite-kyanite granulite xenoliths from Lashaine, Tanzania, *J. Geol.*, *91*, 143–165.

Jones, C. H., K. H. Mahan, L. A. Butcher, W. B. Levandowski, and G. L. Farmer (2015), Continental uplift through crustal hydration, *Geology*, *43*(4), 355–358.

Julià, J., and A. A. Nyblade (2013), Probing the upper mantle transition zone under Africa with P520s conversions: Implications for temperature and composition, *Earth Planet. Sci. Lett.*, *368*, 151–162.

Karlstrom, L., J. Dufek, and M. Manga (2009), Organization of volcanic plumbing through magmatic lensing by magma chambers and volcanic loads, *J. Geophys. Res.*, *114*, B10204, doi:10.1029/2009JB006339.

Keir, D., C. Ebinger, E. Daly, G. Stuart, P. Maguire, and A. Ayele (2006a), Strain accommodation by magmatism and faulting as rifting proceeds to breakup: Seismicity of the northern Ethiopian rift, *J. Geophys. Res.*, *111*, B05314, doi:10.1029/2005JB003748.
Keir, D., G. W. Stuart, A. Jackson, and A. Ayele (2006b), Local earthquake magnitude scale and seismicity rate for the Ethiopian rift, *Bull. Seismol. Soc. Am.*, *96*(6), 2221–2230.
Keir, D., I. D. Bastow, K. A. Whaler, E. Daly, D. G. Cornwell, and S. Hautot (2009), Lower crustal earthquakes near the Ethiopian rift induced by magmatic processes, *Geochem. Geophys. Geosyst.*, *10*, Q0AB02, doi:10.1029/2009GC002382.
Kendall, J. M., and C. Lithgow-Bertelloni (2016), Why is Africa rifting?, *Geol. Soc. Spec. Publ.*, *420*(1), 11–30.
Keranen, K., S. L. Klemperer, and R. Gloaguen, and EAGLE Working Group (2004), Three-dimensional seismic imaging of a protoridge axis in the Main Ethiopian rift, *Geology*, *32*(11), 949–952.
Kervyn, M., G. G. Ernst, J. Keller, R. G. Vaughan, J. Klaudius, E. Pradal, F. Belton, H. B. Mattsson, E. Mbede, and P. Jacobs (2010), Fundamental changes in the activity of the natrocarbonatite volcano Oldoinyo Lengai, Tanzania, *Bull. Volcanol.*, *72*(8), 913–931.
Klein, F. W. (2002), User's guide to HYPOINVERSE-2000, a Fortran program to solve for earthquake locations and magnitudes, *Rep. 2002–171*, U.S. Geol. Surv., Menlo Park, Calif.
Kostrov, V. V. (1974), Seismic moment and energy of earthquakes, and seismic flow of rock, *Izv. Acad. Sci. USSR Phys. Solid Earth*, *1*, 23–44.
Langston, C. A., R. Brazier, A. A. Nyblade, and T. J. Owens (1998), Local magnitude scale and seismicity rate for Tanzania, East Africa, *Bull. Seismol. Soc. Am.*, *88*(3), 712–721.
Le Gall, B., P. Nonnotte, J. Rolet, M. Benoit, H. Guillou, M. Mousseau-Nonnotte, J. Albaric, and J. Deverchère (2008), Rift propagation at craton margin: Distribution of faulting and volcanism in the North Tanzanian Divergence (East Africa) during Neogene times, *Tectonophysics*, *448*(1), 1–19.
Lee, H., J. D. Muirhead, T. Fischer, C. J. Ebinger, S. Kattenhorn, and G. Kianji (2016), Massive and prolonged deep carbon emissions associated with continental rifting, *Nat. Geosci.*, *9*, 145–149.
Lee, H., T. Fischer, J. D. Muirhead, C. J. Ebinger, S. A. Kattenhorn, Z. D. Sharp, G. Kianji, Y. Sano, and N. Takahata (2017), Incipient rifting accompanied by the release of subcontinental lithospheric mantle volatiles in the Magadi and Natron basin, East Africa, *J. Volcanol. Geotherm. Res.*, doi:10.1016/j.jvolgeores.2017.03.017, in press.
Lindenfeld, M., G. Rümpker, K. Link, D. Koehn, and A. Batte (2012), Fluid-triggered earthquake swarms in the Rwenzori region, East African Rift—Evidence for rift initiation, *Tectonophysics*, *566*, 95–104.
Maccaferri, F., E. Rivalta, D. Keir, and V. Acocella (2014), Off-rift volcanism in rift zones determined by crustal unloading, *Nat. Geosci.*, *7*(4), 297–300.
Main, I. G. (1987), A characteristic earthquake model of the seismicity preceding the eruption of Mount St. Helens on 18 May 1980, *Phys. Earth Planet. Inter.*, *49*(3–4), 283–293.
Mana, S., T. Furman, B. D. Turrin, M. D. Feigenson, and C. C. Swisher (2015), Magmatic activity across the East African North Tanzanian Divergence Zone, *J. Geol. Soc.*, *172*, 368.
Manega, P. C. (1993), Geochronology, geochemistry and isotopic study of the Plio-Pleistocene hominid sites and the Ngorongoro volcanic highland in northern Tanzania, PhD thesis, 267 pp., Univ. Colo. Boulder.
Mansur, A.T., S. Manya, S. Timpa, and R. L. Rudnick (2014), Granulite-facies xenoliths in rift basalts of Northern Tanzania: Age, composition and origin of Archean lower crust, *J. Petrol.*, *55*(7), 1243–1286.
Manya, S. (2014), Geochemistry of the Palaeoproterozoic gabbros and granodiorites of the Saza area in the Lupa Goldfield, southwestern Tanzania, *J. Afr. Earth Sci.*, *100*, 401–408.
Manya, S., and M. A. H. Maboko (2003), Dating basaltic volcanism in the Neoarchaean Sukumaland Greenstone Belt of the Tanzania Craton using the Sm–Nd method: Implications for the geological evolution of the Tanzania Craton, *Precambrian Res.*, *121*(1), 35–45.
Mattsson, H. B., and B. A. Tripoli (2011), Depositional characteristics and volcanic landforms in the Lake Natron–Engaruka monogenetic field, northern Tanzania, *J. Volcanol. Geotherm. Res.*, *203*(1), 23–34.
Mattsson, H. B., R. H. Nandedkar, and P. Ulmer (2013), Petrogenesis of the melilititic and nephelinitic rock suites in the Lake Natron–Engaruka monogenetic volcanic field, northern Tanzania, *Lithos*, *179*, 175–192.
McHenry, L. J., L. Luque, J. Á. Gómez, and F. Diez-Martín (2011), Promise and pitfalls for characterizing and correlating the zeolitically altered tephra of the Pleistocene Peninj Group, Tanzania, *Quat. Res.*, *75*(3), 708–720.
Mollel, G. F., C. C. Swisher III, M. D. Feigenson, and M. J. Carr (2008), Geochemical evolution of Ngorongoro Caldera, Northern Tanzania: Implications for crust–magma interaction, *Earth Planet. Sci. Lett.*, *271*(1), 337–347.
Mollel, G. F., C. C. Swisher III, M. D. Feigenson, and M. J. Carr (2011), Petrology, geochemistry and age of Satiman, Lemagurut and Oldeani: Sources of the volcanic deposits of the Laetoli area, in *Paleontology and Geology of Laetoli: Human Evolution in Context*, pp. 99–119, Springer, Dordrecht, Netherlands.
Mudd, G. C., and G. R. Orridge (1966), *Babati 1:250 000 Map Sheet*, Miner. Resour. Div., Dodoma.
Muirhead, J. D., S. A. Kattenhorn, and N. Le Corvec (2015), Varying styles of magmatic strain accommodation in the East African Rift, *Geochem. Geophys. Geodyn.*, *16*, 2775–2795.
Muirhead, J. D., S. A. Kattenhorn, H. Lee, T. P. Fischer, S. Mana, B. Turrin, G. Kianji, E. Dindi, and D. S. Stamps (2016), Evolution of upper crustal faulting assisted by magmatic volatile release during early-stage continental rift development in the East African Rift, *Geosphere*, *12*, 1670, doi:10.1130/GES01375.1.
Mulibo, G. D., and A. A. Nyblade (2009), The 1994–1995 Manyara and Kwamtoro earthquake swarms: Variation in the depth extent of seismicity in Northern Tanzania, *S. Afr. J. Geol.*, *112*(3–4), 387–404.
Mulibo, G. D., and A. A. Nyblade (2013), Mantle transition zone thinning beneath eastern Africa: Evidence for a whole-mantle superplume structure, *Geophys. Res. Lett.*, *40*, 3562–3566, doi:10.1002/grl.50694.
Niemeijer, A. R., and C. J. Spiers (2005), Influence of phyllosilicates on fault strength in the brittle-ductile transition: Insights from rock analogue experiments, *Geol. Soc. Spec. Publ.*, *245*(1), 303–327.
Novak, O., J. R. R. Ritter, R. Altherr, V. Garasic, F. Volker, C. Kluge, T. Kaspar, G. F. Byrne, S. V. Sobolev, and K. Fuchs (1997), An integrated model for the deep structure of the Chyulu Hills volcanic field, Kenya, *Tectonophysics*, *278*, 187–209.
Nyblade, A. A., and C. A. Langston (1995), East African earthquakes below 20 km depth and their implications for crustal structure, *Geophys. J. Int.*, *121*(1), 49–62.
Nyblade, A. A., and S. W. Robinson (1994), The African Superswell, *Geophys. Res. Lett.*, *21*, 765–768.
Oliva, S., C. J. Ebinger, D. Shillington, J. Albaric, A. Deschamps, D. Keir, and C. Drooff (2017), Comparison of magmatic and amagmatic rift zone kinematics using full moment tensor inversions of regional earthquakes, *Geophys. Res. Abstr.*, *19*, EGU2017–941.
Pik, R., B. Marty, and D. R. Hilton (2006), How many mantle plumes in Africa? The geochemical point of view, *Chem. Geol.*, *226*(3), 100–114.

Plasman, M., et al. (2017), Lithospheric low-velocity zones associated with a magmatic segment of the Tanzanian Rift, East Africa, *Geophys. J. Int.*, *210*(1), 465–481.
Reyes, C. G., and M. E. West (2011), The waveform suite: A robust platform for manipulating waveforms in MATLAB, *Seismol. Res. Lett.*, *82*(1), 104–110.
Reyners, M., D. Eberhart-Phillips, and G. W. Stuart (2007), The role of fluids in lower-crustal earthquakes near continental rifts, *Nature*, *446*(7139), 1075–1078.
Richter, C. F. (1958), *Elementary Seismology*, 768 pp., W. H. Freeman, San Francisco, Calif.
Ring, U. W. E., H. L. Schwartz, T. G. Bromage, and C. Sanaane (2005), Kinematic and sedimentological evolution of the Manyara Rift in northern Tanzania, East Africa, *Geol. Mag.*, *142*(4), 355–368.
Ritsema, J., H. J. van Heijst, and J. H. Woodhouse (1999), Complex shear wave velocity structure imaged beneath Africa and Iceland, *Science*, *286*(5446), 1925–1928.
Roecker, S., et al. (2017), Subsurface images of the Eastern Rift, Africa, from the joint inversion of body waves, surface waves and gravity: Investigating the role of fluids in early-stage continental rifting, *Geophys. J. Int.*, *210*(2), 931–950.
Saria, E., E. Calais, Z. Altamimi, P. Willis, and H. Farah (2013), A new velocity field for Africa from combined GPS and DORIS space geodetic Solutions: Contribution to the definition of the African reference frame (AFREF), *J. Geophys. Res. Solid Earth*, *118*, 1677–1697, doi: 10.1002/jgrb.50137.
Schmandt, B., and E. Humphreys (2010), Seismic heterogeneity and small-scale convection in the southern California upper mantle, *Geochem. Geophys. Geosyst.*, *11*, Q05004, doi:10.1029/2010GC003042.
Scholz, C. H. (1968), The frequency-magnitude relation of microfracturing in rock and its relation to earthquakes, *Bull. Seismol. Soc. Am.*, *58*(1), 399–415.
Scholz, C. H. (2015), On the stress dependence of the earthquake b value, *Geophys. Res. Lett.*, *42*, 1399–1402, doi:10.1002/2014GL062863.
Selverstone, J., and T. Wawrzyniec (2001), High-temperature embrittlement of extensional Alpine mylonite zones in the midcrustal ductile-brittle transition, *J. Geophys. Res.*, *106*, 4337–4348.
Selway, K., J. Yi, and S. I. Karato (2014), Water content of the Tanzanian lithosphere from magnetotelluric data: Implications for cratonic growth and stability, *Earth Planet. Sci. Lett.*, *388*, 175–186.
Sherrod, D., M. Magigita, and S. Kwelwa (2013), Geologic map of Oldonyo Lengai (Oldoinyo Lengai) volcano and surroundings, Arusha region, United Republic of Tanzania, *U.S. Geol. Surv. Open File Rep*. 2013-1306, GIS database, 1 sheet, scale 1:50,000, 65 pp. Available at http://dx.doi.org/10.3133/ofr20131306.
Shudofsky, G. N. (1985), Source mechanisms and focal depths of East African earthquakes using Rayleigh-wave inversion and body-wave modelling, *Geophys. J. Int.*, *83*(3), 563–614.
Sibson, R. H. (1992), Implications of fault-valve behaviour for rupture nucleation and recurrence, *Tectonophysics*, *211*(1–4), 283–293.
Sippel, J., C. Meeßen, M. Cacace, J. Mechie, S. Fishwick, C. Heine, M. Scheck-Wenderoth, and M. R. Strecker (2017), The Kenya rift revisited: Insights into lithospheric strength through data-driven 3-D gravity and thermal modelling, *Solid Earth*, *8*(1), 45.
Smith, M., and P. Mosley (1993), Crustal heterogeneity and basement influence on the development of the Kenya Rift, East Africa, *Tectonics*, *12*, 591–606.
Snoke, J. A., J. W. Munsey, A. G. Teague, and G. A. Bollinger (1984), A program for focal mechanism determination by combined use of polarity and SV-P amplitude ratio data, *Earthquake Notes*, *55*, 920211.
Stammler, K. (1993), SeismicHandler—Programmable multichannel data handler for interactive and automatic processing of seismological analyses, *Comput. Geosci.*, *19*(2), 135–140.
Thompson, D. A., J. O. S. Hammond, J. M. Kendall, G. W. Stuart, G. R. Helffrich, D. Keir, A, Ayele, and B. Goitom (2015), Hydrous upwelling across the mantle transition zone beneath the Afar Triple Junction, *Geochem. Geophys. Geosyst.*, *16*, 834–846, doi:10.1002/2014GC005648.
Thybo, H., and I. M. Artemieva (2013), Moho and magmatic underplating in continental lithosphere, *Tectonophysics*, *609*, 605–619.
Thybo, H., P. K. H. Maguire, C. Birt, and E. Perchuć (2000), Seismic reflectivity and magmatic underplating beneath the Kenya Rift, *Geophys. Res. Lett.*, *27*, 2745–2748.
Tongue, J., P. K. H. Maguire, and P. Burton (1994), An earthquake study in the Lake Baringo basin of the central Kenya Rift, *Tectonophysics*, *236*(1–4), 151–164.
Utsu, T. (1965), A method for determining the value of *b* in formula $\log N = a - bM$ showing the magnitude-frequency relation for earthquakes, *Geophys. Bull. Hokkaido Univ.*, *13*, 99–103.
Vauchez, A., F. Dineur, and R. L. Rudnick (2005), Microstructure, texture and seismic anisotropy of the lithospheric mantle above a mantle plume: Insights from the Labait volcano xenoliths (Tanzania), *Earth Planet. Sci. Lett.*, *232*(3), 295–314.
Wada, I., M. D. Behn, and A. M. Shaw (2012), Effects of heterogeneous hydration in the incoming plate, slab rehydration, and mantle wedge hydration on slab-derived H_2O flux in subduction zones, *Earth Planet. Sci. Lett.*, *353*, 60–71.
Waldhauser, F., and W. L. Ellsworth (2000), A double-difference earthquake location algorithm: Method and application to the northern Hayward fault, California, *Bull. Seismol. Soc. Am.*, *90*, 1353–1368.
Wang, Y. F., J. F. Zhang, J. M. Jin, and H. W. Green (2012), Mafic granulite rheology: Implications for a weak continental lower crust, *Earth Planet. Sci. Lett.*, *353*, 99–107.
Wauthier, C. (2011), Radar interferometry (InSAR) applied to the study of active volcanic and seismic areas in Africa, PhD dissertation, 245 pp., Univ. of Liege, Liege, Germany.
Wessel, P., and W. H. Smith (1998), New, improved version of Generic Mapping Tools released, *Eos Trans. AGU*, *79*(47), 579–579.
Wiemer, S., S. R. McNutt, and M. Wyss (1998), Temporal and three-dimensional spatial analyses of the frequency–magnitude distribution near Long Valley Caldera, California, *Geophys. J. Int.*, *134*(2), 409–421.
Woessner, J., and S. Wiemer (2005), Assessing the quality of earthquake catalogues: Estimating the magnitude of completeness and its uncertainty, *Bull. Seismol. Soc. Am.*, *95*(2), 684–698.
Yang, Z., and W. P. Chen (2010), Earthquakes along the East African Rift System: A multiscale, system-wide perspective, *J. Geophys. Res.*, *115*, B12309, doi:10.1029/2009JB006779.